Improved understanding of the behaviour of mercury and other trace metals in basaltic magmas

Laura Garcia Ramos

MSc by research in Earth Sciences

Department of Earth Sciences & St. Hugh's College at the University of Oxford

Supervisors: Prof. Tamsin A. Mather & Prof. Bernard J. Wood

Project funded by the European Research Council & the Burdett Coutts fund

St Hugh's College
UNIVERSITY OF OXFORD

ABSTRACT

Volcanic degassing is one of the major emission sources in nature for atmospheric mercury, and the only one able to directly reach the stratosphere and troposphere. The actual magnitude of these emissions remains uncertain, due to the difficulties of accurately measuring the Hg from active volcanoes and the lack of published mercury analysis in volcanic rocks. It is critical to improve our knowledge on volcanic Hg behaviour and emissions to be able to establish the impact of these in the current and past atmospheric mercury budget. For that purpose, we need to understand how the volatility of mercury is affected under different conditions in a degassing volcano. This thesis attempts to overcome the difficulties of obtaining in- situ mercury analysis by producing, at high temperatures and pressures basaltic melts doped in mercury and other volatiles. There is no prior experimental record on mercury at high-temperature, due to the high volatility of this element, therefore, I have tested several experimental conditions and materials to counteract the evaporation of mercury during the synthesis of the glass and/or sulfide. These involve single-capsule and double-capsule assemblies. Additionally, I have performed a series of sulfide-silicate partitioning experiments for pressures ranging from 0.5 GPa to 2 GPa. These experiments seek to determine the pressure effect on the distribution of Ag, Cd, Co, Cr, Cu, Ga, Ge, In, Pb, Se, Sb, Tl, V, and Zn between both phases, and thus enhance the existing partitioning model that only considers melt and sulfide composition and temperature, as parameters.

Acknowledgements:

The realization of this study has been possible thanks to the guidance and supervision of Professor Tamsin Mather and Professor Bernard Wood, as well as the helpful advice of Dr Andrew Matzen, and the rest of the Experimental Petrology group. I am thankful for the financial support of the ERC and the Burdett Coutts fund.

LIST OF FIGURES

LIST OF TABLES

TABLE OF CONTENTS

Chapter 1. Introduction: Relevance of mercury degassing, gaps and challenges.

Volcanic activity releases substantial quantities of trace elements into the atmosphere through magmatic degassing processes (e.g., Allard *et al.*, 2000; Hinkley *et al.*, 1999; Mather *et al.*, 2012), which contribute significantly to the environmental reservoir of these. Trace-metals play a role in some biogeochemical cycles, as well as promoting the bio-productivity of certain species (Olgun *et al.*, 2013). However, these erupted substances include highly toxic elements that may enter living organisms through not only inhalation but also food consumption. Heavy metals are absorbed in the tissues of different species and passed through the food chain, increasing their concentration through bioaccumulation (e.g., Pb and Cd, Vinodhini & Narayanan 2008; Pb, Cd and Cu, Heikens et al., 2001; Hg, Bargagli 2008).

This study focuses on Hg, an element of very high toxicity, that has been progressively accumulating in the atmosphere due to both anthropogenic and natural causes: its atmospheric concentration has increased by more than three times since the industrial revolution (Mason *et al.*, 1994; UNEP 2013), with estimates ranging from 842 Mg yr^{-1} (Pirrone *et al.*, 2010) to 2500 ± 500 Mg yr^{-1}, (Outridge *et al.,* 2018). While human activities have an undeniable impact on these figures, natural sources are estimated to have an equal contribution (Outridge *et al.*, 2018). Volcanic emissions are one of the most important natural sources of Hg, but

the amount of Hg released in these emissions is not well constrained, and estimates vary from 0.1 to 1000 Mg yr^{-1}; for example, Bagnato *et al.,* (2015) estimated 76 ± 30 Mg yr^{-1} including only quiescent volcanic degassing, Witt *et al.,* (2008) estimated 74 Mg yr^{-1} from basaltic volcanoes by extrapolation of in-situ measurements on Masaya volcano, and Pyle & Mather (2003) estimated ~700 Mg yr^{-1} based on published data on active volcanoes. On top of that, Hg emissions might be dependent on the geotectonic setting of the eruption, with Hg influx from arc volcanoes estimated to be three times greater than that of non-arc volcanoes (Edwards et al., 2020). This could be a consequence of the volatilisation of Hg from subducting crustal material, which is relatively rich in mercury (30 ppb Hg, Rudnick & Gao 2014) under the increasing temperature (Bagnato *et al.*, 2015 and references therein; Coufalík *et al.*, 2018; Edwards *et al.,* 2020), however, there is not yet a definite answer to this apparent difference. The inconsistency of estimates is a significant drawback to understanding the natural Hg cycle, and an obstacle to planning actions to mitigate anthropogenic Hg emissions (Edwards *et al.,* 2020).

Determining how much and in which conditions Hg is released and distributed globally is pressing: mercury poses a severe risk to the human population and marine ecosystems (WHO 2003), particularly in the form of methylated organic mercury (MeHg, CH_3Hg^+). In marine ecosystems, organic mercury enters the ecological chain and severely affects aquatic biota, as it accumulates in different organisms and amplifies trophic levels, eventually being introduced into the human body, often via fish consumption (e.g., Perrault *et al.*, 2014).

However, Hg has also been identified as a valuable chemostratigraphic tracer. Mercury is typically sequestered by organic matter in marine environments, and therefore, concentration spikes in sediments could represent an overwhelming influx of this element into the atmosphere from the elevated rates of volcanism, as in the case of Large Igneous Provinces or "LIP" (Grasby *et al.*, 2016). Following this reasoning, the presence of high Hg to low Total Organic Carbon (T.O.C.) ratios, predating or synchronous to all five major extinction horizons (Sanei *et al.*, 2012; Grasby *et al.*, 2016; Bond & Grasby 2017; Percival *et al.*, 2018; Clapham & Renne 2019; Racki, 2020) might be linked to LIP-synchronous mass extinction events. The relationship between sedimentary Hg anomalies and LIP events has been explored and supported by several studies (Sanei *et al.*, 2012; Percival *et al.*, 2018; Jones *et al.*, 2019; Racki, 2020 and references therein). Nonetheless, Hg anomalies do not correlate with all LIP events. Specifically, they seem to be related to LIPs that include the following characteristics: subaerial volcanism, explosive eruptions, and the production of thermogenic volatiles (Percival *et al.,* 2015; Percival *et al.*, 2018; Grasby *et al.,* 2019; Racki 2020). To establish sedimentary Hg as a reliable tracer, further work is needed to understand how Hg is affected by the different volcanic processes and geotectonic settings.

Unfortunately, our current knowledge of volcanic mercury fluxing is still scarce. Measurements are focused on a limited number of major emitters, such as Etna and Kilauea volcanoes, which provide only a partial view of global emissions (Bagnato *et al.*, 2007; Mather 2015; Edwards *et al.*, 2020). Furthermore, *in-situ* acquisition of

data is fairly limited, due to the difficulty in operating analytical equipment on volcanoes. This problem has been eased with the increase in usage of portable 915+ Lumex direct mercury analysers (Lumex Instruments, St. Petersburg, Russia). This device can perform real-time identification of the Hg concentrations through AAS (Atomic Absorption Spectrometry) and allows for several hours of measurements (Kim *et al.*, 2006) thus enabling continuous data logging of the element (Edwards et al., 2020). However, the scope of this analytical device is limited to Gaseous Elemental Mercury (GEM) or Hg^0. Volcanic mercury emissions consist of TGM (Total Gaseous Mercury) and particulate mercury ($Hg_{(p)}$). TGM is further divided into GEM (Hg^0) and Reactive Gaseous Mercury (RGM) or Hg^{II}. While there is supported evidence that most of the TGM consists of GEM (e.g.: Landis *et al.,* 2002; Witt *et al.,* 2008; Bagnato *et al.,* 2017), the proportion of RGM might vary in different eruptions and needs to still be accounted for. Gold-coated sand traps are used for collecting both GEM and RGM, whereas KCl denuders might be used for acquiring only RGM (Landis *et al.,* 2002). Particulate mercury can be obtained through quartz microfiber mini traps (Witt *et al.,* 2008). However, the referenced collecting techniques besides the Lumex are more time-constrained, and they are not able to perform analyses, with samples needing to be subsequently stored and analysed.

Data from explosive eruptions are even more complex to obtain due to the challenge of collecting samples in such conditions. Sporadic eruptions have been estimated to add up to 75% of total volcanic Hg emissions, while the more infrequent and large explosive eruptions would constitute ~15% (Pyle & Mather 2003). In particular,

these odd, large explosive eruptions are almost entirely injected into the stratosphere and provoke great perturbations in the atmospheric mercury reservoir (Pyle & Mather 2003). Therefore, improving the estimated values for these emissions is essential to understanding the actual contributions of volcanic activity.

Current estimates of volcanic Hg emissions are based on plume Hg/SO_2 ratios, and Hg/CO_2 ratios in settings in which SO_2 concentrations are low (e.g., fumaroles and diffuse emissions seeping through soils, Bagnato *et al.*, 2014). Comparing mercury concentrations to SO_2 can cause misleading Hg emission values, since the Hg/SO_2 ratios in a given plume will change during degassing, due to the fractionation of both as they incorporate in silicate melts differently (Bagnato *et al.*, 2015). Furthermore, volcanoes that belong to the same geotectonic setting may show different $Hg\text{-}SO_2$ patterns, due to the influence of certain halogens (e.g., F, I, Cl) on the speciation of Hg (Mather *et al.*, 2012).

Because of these uncertainties, there is an obvious need to improve our knowledge of the behaviour of Hg in pre-eruptive melts and of the factors that influence its degassing. Mercury is highly volatile, and it readily incorporates into the gaseous phase at high temperatures. As a result, it is barely present in the solid products of a volcanic eruption. In fact, the low concentration of this element and the difficulties that involve its analysis translate into the almost complete absence of mercury measurements for basaltic rocks. Only a small number of studies include Hg measurements in their trace-element analysis. Conversely, when Hg is measured, the rest of trace-element analysis is often not listed with it, thus impeding the search

for any potential elemental correlation between mercury and other traces. The increasing use of direct mercury analysers (DMA-80, Milestone; Lumex RA-915) will hopefully improve the availability of this data in the future.

However, there is another way of increasing our knowledge of this topic that has not been explored due to its challenging nature, and that is the application of experimental petrology to generate the data we cannot easily obtain in nature. There is a complete absence of any record of experimental attempts at reproducing high-temperature settings to observe Hg behaviour. This is due to its mentioned high volatility that hinders the synthesis of a mercury-doped glass at high temperature.

This MSc (Res) project aimed to create synthetic glasses of basaltic composition, containing a selected amount of Hg and other trace elements, in order to ultimately empirically obtain the volatility coefficient of Hg under different experimental conditions. For these volatility experiments to be conducted, we need to first develop an experimental methodology that will allow us to systematically produce mercury-doped glasses and find a reliable analytical technique to measure mercury concentrations in the glass. A number of sample cells and mixtures have been tested with very small success (Figure 1), which will be described in chapter 3**.** At the current stage, we are unable to satisfactorily retain the initial concentration of mercury in the mixture after melting or to obtain a consistent pattern of evaporation loss in our samples, however, these attempts have provided some insights into what temperature range and sleeve and capsule material would be more adequate to

maximise retention, as well as which analytical techniques should be used for an accurate determination of total mercury concentration.

Along with mercury volatility, I studied the impact of sulfides in the preservation and distribution of mercury between two immiscible liquids of sulfide and silicate compositions. As Mercury is chalcophile ("sulfur loving"), it is likely to be critically impacted by the presence of sulfides in the magma. MORBs, which are sulfide saturated (Smythe *et al.,* 2017), are common in LIP type events. Therefore, as the Hg—S interactions might significantly influence the degassing of this element, it is also important to determine how this element distributes between silicate and sulfide melts at high-temperature/high-pressure conditions, at equilibrium. To observe this process, I performed several experiments *via* a piston-cylinder press (Boyd & England 1960) and measure the concentration of Hg in both phases in the final melt. This data will also contribute to the improvement of the thermodynamic model developed in Kiseeva & Wood (2013; 2015) for chalcophile and lithophile elements into sulfide melt. This model (Kiseeva & Wood 2013) establishes that the sulfide-silicate partitioning coefficient ($D_M^{Sulf/Sil}$) of a given trace-element M and the concentration of FeO in the silicate phase is related to the FeO concentration in the silicate through the following expression:

$$log\left(D_M^{Sulf/Sil}\right) \approx A + \frac{n}{2} log[FeO]_{silicate} \qquad \text{(eq. 1)}$$

Where A is a constant related to the free energy of the $Fe_{\ sulfide} - M_{silicate}$ exchange reaction, n is a constant related to the valence of the element ($n \sim -1$ for

$+1$ ions, $n \sim -2$ for $+2$ ions, etc.), and $[FeO]_{silicate}$ is the FeO content in the silicate, expressed in wt% or mol % (See chapter 4. section 1)

The experiments carried out here had the goal to account for the effect of pressure by testing its effect on a set of selected trace elements. The pressure-effect was tested by reproducing the methodology described in Kiseeva & Wood (2013; 2015) at different pressures for a small temperature range, for a silicate mixture with chalcophile, lithophile, and siderophile elements.

The better the understanding we acquire from the behaviour of these elements in the different magmatic scenarios, the more accurately we will be able to reconstruct the magmatic history of these elements from their distribution and abundance in natural samples. Ultimately, given that Hg shares many chemical properties with other chalcophiles (affinity to the sulfide phase, high volatility, similar atomic number in the case of Tl, Pb or Bi, etc.), there is a chance that the behaviour of some of them could be comparable to that of Hg, too. Therefore, comparing these elements could help find a useful proxy for mercury.

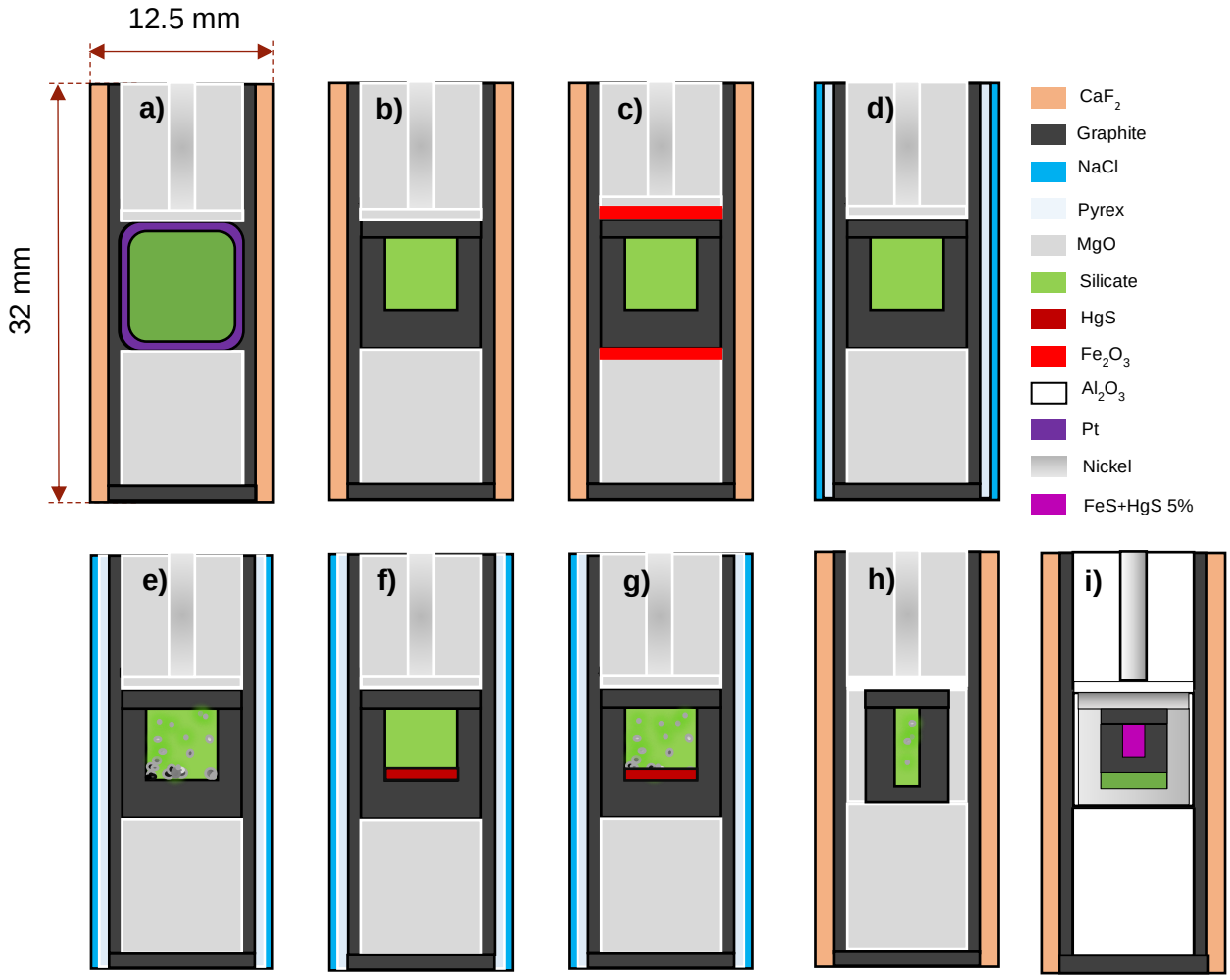

Figure 1. Cross-section of all the sample cells used for the different piston cylinder experiments.

Chapter 2. Preliminary tests: Analytical techniques and optimisation of measurements.

2.1. Assessment of LA-ICP-MS to measure Hg concentration in basalts.

Before attempting any sort of volatilisation or partitioning experiment, we need to establish a consistent and accurate way to measure mercury concentrations in melts. That is, we need an analytical technique that will provide reliable measurements that agree with the concentrations expected in the standards/samples, that is easily reproducible, and coherent through a series of measurements, can yield results relatively rapidly, and is not affected by interferences with other elements. We evaluated the capacity of Laser Ablation Inductively Coupled Plasma Mass Spectrometry (LA-ICP-MS) first, as it can perform (almost) non-destructive analysis of specific spots in the sample, can target specific phases via spot measurements, provides detailed data for most elements in the periodic table, can process several samples during a single session, and requires almost no preparation other than a rough polish of the surface of the samples.

To test the capacity of LA-ICP-MS, we prepared a series of mixtures of Icelandic basalt (Norris 2016) and analytical grade HgO powder at different concentrations: 100,000, 10,000, 1,000, 660, 100, 66, 33, 10, 6.6, and 3.3 ppm HgO. The powders were finely ground with an agate mortar, mixed with PVA, dried at 110ºC for 2h, and pressed into pellets of 2 mm diameter. The pellets were mounted in acrylic resin and polished down to 3µm with synthetic diamond grease and ethanol. In a successful outcome scenario, the different concentrations should show an increase

in detected counts per second (c.p.s.), correlated to the increasing concentration. Since the pellets were made from raw, unheated HgO and rock powder, if any loss of Hg occurred, it would be due to volatilisation induced by the high temperatures reached during ablation.

We also tested a preliminary run of our future high-temperature/high-pressure experiments on the piston-cylinder press, by loading a 1 wt% HgO-bearing Icelandic basalt mixture (IBC0/ glass A000, Table 1) in a platinum capsule. The capsule was welded and placed in the centre of a graphite tube furnace of 8 mm O.D. and 6 mm I.D. –outer and inner diameter, respectively –supported by a pedestal of crushable MgO, and a MgO piece with a 1.6 mm cast hole, on top of it. All of the pieces were custom-made to be tightly fitted. The graphite furnace works as a uniform electric heat generator within the sample cell. The assembly was set inside a 12.5 mm O.D., 8 mm I.D CaF_2 pressure medium (Figure 1. h.), which supports the assembly while transmitting the pressure exerted through the experiment to the capsule (Vlach *et al.,* 2019). The sleeves were manufactured from a CaF_2-PVA powder mixture, pressed, and then fired at 800^{o} C for 20-25 minutes at 1 atm in a box furnace to get rid of the PVA glue. The assembly was wrapped in thin Pb foil (<0.05 mm), to minimise the effect of friction —this friction can increase the actual pressure upon the capsule and needs to be corrected ("friction-correction", McDade *et al.,* 2002). The temperature of the capsule was monitored throughout the experiment with a fitted C-type $W_{95}Re_5$–$W_{74}Re_{26}$ thermocouple threaded inside a four-bore custom-made insulator. The thermocouple was connected to the upper surface of the

capsule through the drilled MgO piece. A MgO-disc insulator of ~0.5 mm thickness was placed on top of the Pt capsule.

The Pt capsule was welded prior to the assemblage of the sample cell to ensure that the sample will be in a closed environment and reduce potential contamination. The mixture was melted at 1450º C and 1.5 GPa for 10 minutes —with an end-loaded Boyd-England type piston-cylinder apparatus at the University of Oxford. The resulting glass (A000, Table *2*) was mounted and polished in the same fashion as the pellets, to be analysed under LA-ICP-MS.

All of the LA-ICP-MS analyses were carried out with the PerkinElmer NexION® 300/350 ICP-MS (Perkin-ElmerSCIEX Instruments, Concord, Ontario, Canada) in an argon environment, at the University of Oxford. We measured all samples at a 10Hz repetition rate, and for the powder and glass samples containing 100,000 ppm, 10,000 ppm, 1000 ppm, and 100 ppm, we included 4 spots per order of magnitude at 10Hz. The analyses were calibrated against the reference glass NIST610 and normalised to ^{43}Ca, due to it not having any interferences from other elements. The signal for most of the isotopes and samples often produced a spiky graph, where the greatest peak quickly decreased in height afterwards. This sudden drop after the peak could correlate with the rapid loss of mercury from the sample due to the high temperature of the beam. Therefore, we tested two scenarios, one in which the peak was included (Figure 2. b, c), and another one including only the c.p.s. detected after this peak (Figure 2. a). The datasets (Mean Raw c.p.s. background

subtracted) were plotted against the added mercury and showed positive trends with the increasing added Hg (Figure 2). The linear regressions for both scenarios showed acceptable fits for most isotopes at a 10Hz repetition rate, but the R^2 values were marginally higher for the data series that included the initial peak (Figure 2. b). The dataset including the initial peak also had a greater variance in results for all concentrations below 1 wt % Hg, with average c.p.s. that fall within each other's error (Figure 2. b). The isotope ^{201}Hg produced the best fit in both cases, with this being the fourth most abundant isotope of Hg (13.17% abundance). The analyses performed at 5Hz provided lower regression coefficients (Figure 2. c), however, this included pellets of lower Hg concentration than the former measurements (3.3 ppm to 100 ppm) which might have produced an unreliable signal. Therefore, it is reasonable to assume that the capacity of LA-ICP-MS to measure Hg concentrations is severely limited for mercury contents below 100 ppm.

The 1450º C glass rendered slightly lower c.p.s. values than the powder pellet counterpart for most isotopes, except for ^{196}Hg and ^{198}Hg, as well as a greater standard deviation for most isotopes (Figure 2. d).

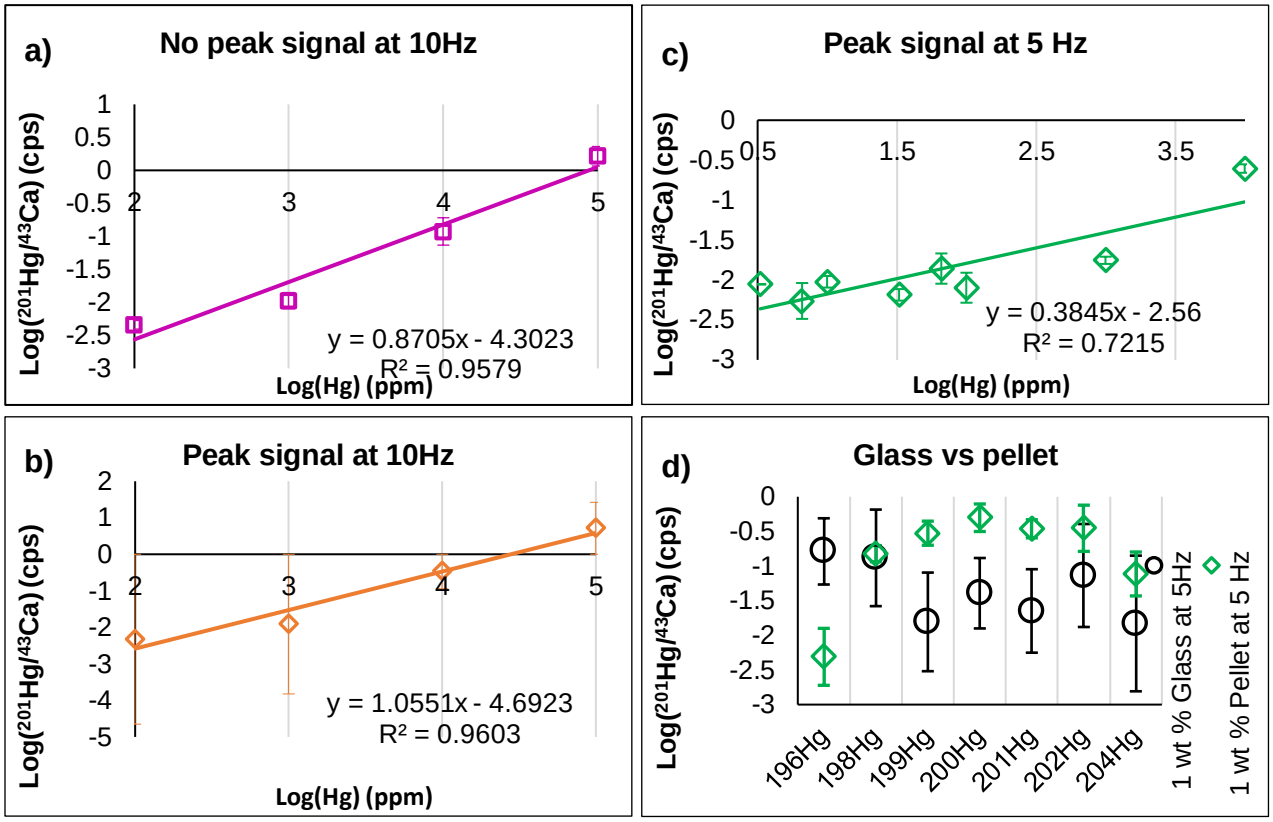

Figure 2. Average log ($^{201}Hg/^{43}Ca$) for the samples containing 100, 1000, 10,000, and 100,000 ppm mercury measured at 10Hz a) not including initial peak, b) including initial peak. c) Average log ($^{202}Hg/^{43}Ca$) for all the powder samples, measured at 5Hz and including the initial peak, d) comparison between the 1 wt. % Hg powder and the 1 wt. % Hg glass measured at 5Hz for every isotope

2.2. Assessment of Lumex RA-915+ multifunctional mercury analyser.

The concentrations of the mixtures containing 10 ppm, 6.6 ppm, and 3.3 ppm, as well as the 1 wt. % Hg in the glass (finely ground), were also determined by thermal decomposition assisted atomic absorption spectrometry (AAS) with the Lumex RA-915+ multifunctional mercury analyser with pyrolysis unit, at the University of Oxford. Four igneous reference samples were analysed including BEN-12, BR-45.5 (Basalts with 12 ppb and 45.5 ppb Hg concentration respectively), GA-56.6, GH155

(Granites with 56.6 ppb and 155 ppb Hg content) —provided by the BCR (Community Bureau of Reference, Brussels). The Hg concentration of these samples had been previously determined *via* AAS with the direct mercury analyser Milestone DMA-80, which includes an amalgamation step (Marie *et al.*, 2015). In addition, we used two NIST sediment standards: 1944 New Jersey Waterway sediment (3.4 ppm Hg) and 2782 Industrial sludge (1.1 ppm Hg) to calibrate the measurements. The basaltic reference samples provided concentrations within 0.2 and 2 ppb from the expected value, whereas the felsic standards recorded values that did not agree with their actual compositions (15.6 to 17.6 ppb less than the expected for GA-56.6 and about 150 ppb less for the GH-155) — such a difference could be due to the coarser grain size observed in the granite standards, as we show later that there is a difference in mercury release in function of grain size (Fostier & Melendez-Perez 2013 and this thesis, section 2.3). The results for the powder mixtures were closer to the experimental compositions: 6.07 ppm for the 10 ppm HgO, 4.55 ppm for the 6.6 ppm HgO, and 3.29 ppm for the 3.3 ppm HgO. However, the A000 glass showed evidence of extensive volatile loss, displaying only 85.2 ppm, indicating a 99.1 % mercury loss over the initial concentration. This loss of Hg suggests that Hg is lost from the experimental setup.

From the concentrations obtained, the Lumex direct mercury analyser provides reliably consistent measurements, as demonstrated by the nearly perfect replication of the results of Marie *et al.,* (2015) for the basalt samples. The low mercury concentration in the glass sample (85.2 ppm, with a Hg loss of 99.1%, Table *2*)

however, seems to signal that the mercury loss occurred during the high temperatures melting.

The Lumex mercury analyzer requires no more preparation of the analyte than grinding the glass into fine powder, and the measurements are obtained within a couple of minutes. The instrument provides exclusively total mercury concentrations, which is advantageous due to the simplicity of data post-processing, but insufficient for more detailed analytical work—spot or line measurements, multi-elemental analysis, etc. The sample is partially combusted during every measurement, which degrades the material and prevents further analysis of the same. Finally, the apparatus cannot bear very high concentrations of mercury, so the input mass needs to be considered in the case of analysing a relatively Hg-rich powder.

For the LA-ICP-MS measurements, while the samples with concentrations over 100 ppm yielded data with good correlations, the samples of lower concentrations did not. Since natural basaltic rocks are hosts of less than ~10 ppb Hg (Canil *et al.,* 2014; Coufalik *et al.,* 2018), this technique might not be as adequate as the Lumex mercury analyzer, which was able to obtain concentrations down to just a few ppb from the tested standards. Additionally, the LA-ICP-MS poses some challenges such as spectral interferences —^{196}Pt, ^{198}Pt, and ^{204}Pb might present as ^{199}Hg, ^{198}Hg, and ^{204}Hg (Wojciechowski *et al.,* 2008), potential volatilization of Hg due to the high temperatures reached during ablation, dispersion of the already low concentration of mercury due to the presence of seven Hg isotopes, and insufficient

ionization of mercury due to the relatively small difference between the ionization potential of Argon (15.76 kJ mol^{-1}) and Hg (10.6 kJ mol^{-1}). Furthermore, LA-ICP-MS is a costly technique that requires greater sample preparation and longer time spent in acquiring the data. On the other hand, the Lumex direct mercury analyser offers a straightforward and fast way of obtaining mercury concentration measurements down to even a few ppb, with virtually no sample preparation. Given the accuracy of the Lumex and its unique advantages, we decided to carry out all future total mercury analyses through this technique.

2.3. Optimization of total mercury measurements with respect to grain size and sample mass.

The signal detected by the Lumex analyser is dependent on grain size. The effect of granulometry in direct mercury analysers has already been tested for soil samples (e.g., Fostier & Melendez-Perez 2013), concluding that finer grain-size fractions produced higher concentrations. Repeated grinding of samples and sieving into different subgroups maximises homogeneity for every sample fraction. The smaller the particle size, the larger surface area to volume ratios, thus allowing more efficient pyrolysis and Hg release. To establish the optimal grain size for our samples, the glasses B001, A001, and A002 (see chapter 3, section 1.1 and table 1 & 2) were sieved into four different grain size fractions: 500 µm, 354 µm, 250 µm, and 125 µm. The results show higher concentrations for grain sizes <354 microns (Table 2), however, some of these data points are within error of each other and therefore the trend is not completely reliable for the grain size-fractions smaller than 354 microns. Two basalt reference standards were used including BEN-12, BR-45.5

— provided by the BCR (Community Bureau of Reference, Brussels). As well as a sedimentary standard containing ~300 ppb Hg.

The glass B001 showed values below 50 ppb for all grain sizes with very small variation for the different grain-size fractions, and a Hg loss percentage of 99.99% (Table 2). This is the only glass product created by melting at 1 atm, and the low concentrations obtained mean that almost all the mercury in the starting composition had evaporated during the experimental run. Additionally, only one measurement per grain-size group was carried out, which lowers the reliability of this relationship.

Despite the small data sample, based on the observations from literature and our results (Figure 3. a), we decided to set the granulometry criteria to ≤ 250-354 µm for all the subsequent experiments.

It is relevant to mention that the process of sieving led to major losses in sample mass during its preparation, due to the high static electricity of the tools employed and the glass particles. The small grains became attached to any surface of the tools employed for handling or processing them, which required a great effort to recover, even in combination with ethanol washes and ultrasonic baths. This extra manipulation likely increased background contamination. In future experiments, using an AC ioniser to neutralise the charge of the tools would reduce these problems significantly (Koizumi *et al.,* 2010).

Ultimately, we need to account for the potential error caused during the grain size fraction's manual separation. Before establishing a proper calibration of grain-size/mercury release, these experiments and sieving should be replicated to create a greater number of data points, as well as accounting for the human and instrumental error.

Regarding the impact of the mass input in the analyser, we calculated the average Hg concentration for every mass input in the analyser. A001 and B001 were only measured one time per grain-size fraction and mass input. However, the concentrations displayed for A002 were averaged from various subgroups of measurements that were carried out with masses ranging from 1 to 6.5 mg. Figure 3. b, seems to show that measured amounts of 1 to 3 mg translate into higher Hg concentration readings than larger mass inputs for the glass A002. However, this skew is not reflected in A001, and it could be explained by the fact that the experiment A002 also retained the most mercury, and that most of the measurements done on mass inputs below 3 mg belong to that sample. The evaluation of the effect of input mass is not conclusive and does not show any reliable trend since both A001 and A002 provide opposite results. Besides, the accuracy of the balance used at such low quantities may be questionable, which could invalidate any judgment for the different mass inputs in the range from 1 to 10 mg. It is noteworthy that for samples with an initial concentration of Hg >1 wt%,

masses much greater than 1 mg could trigger problematic low radiation warnings on the detector, which invalidate the measurement —See chapter 5, section 5.2.2.

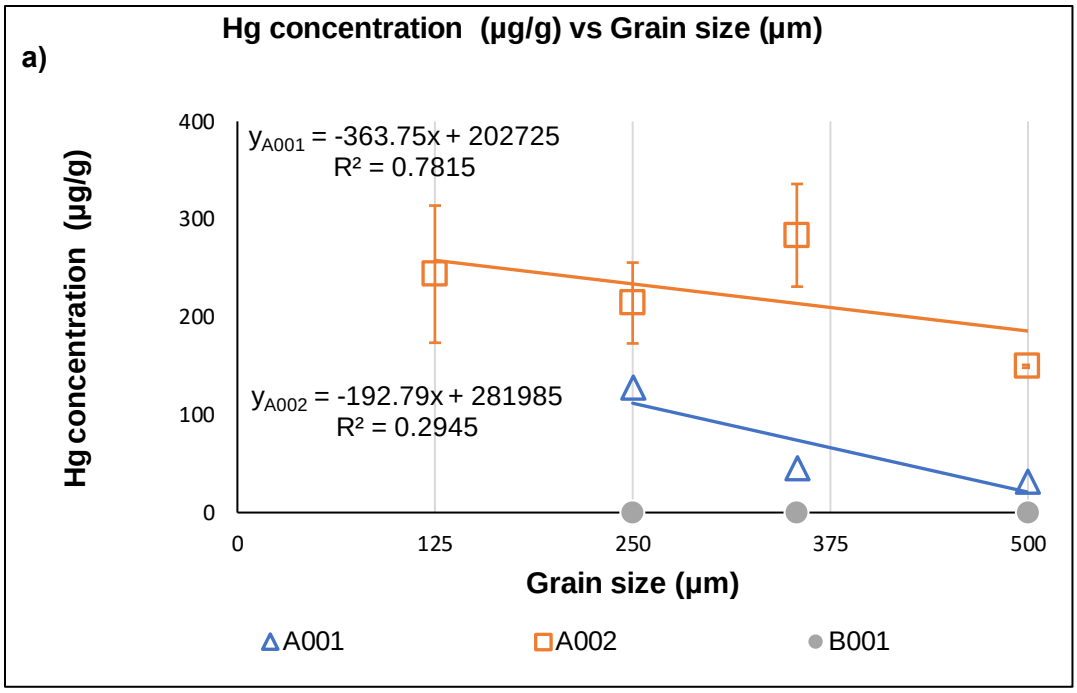

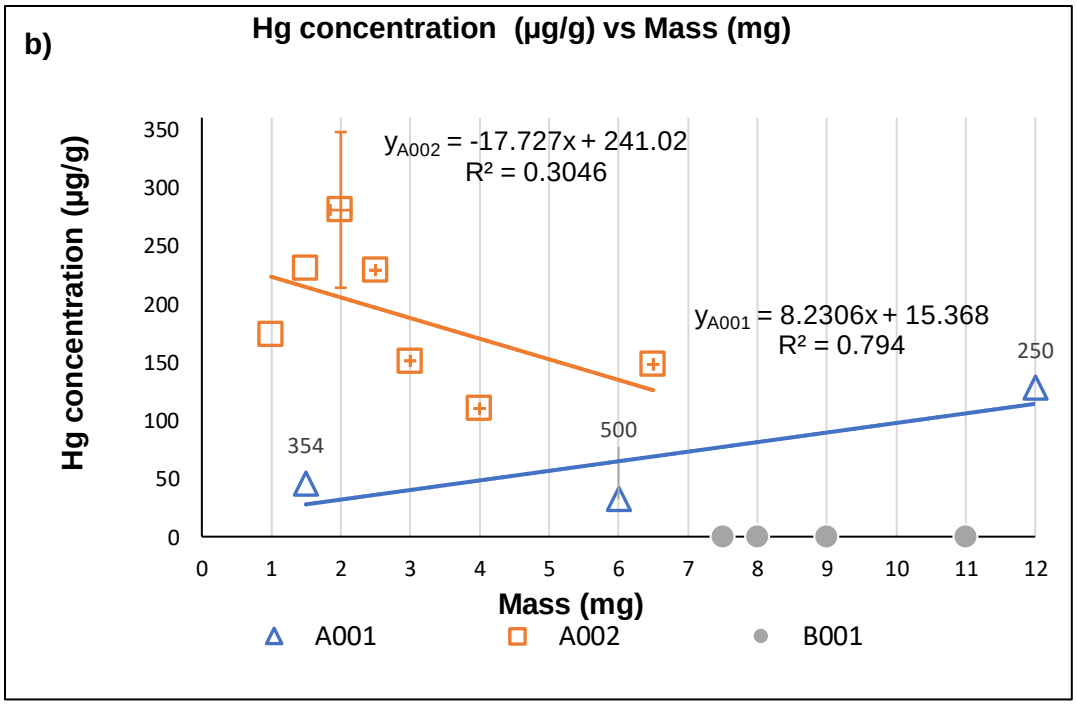

Figure 3. (Above) a) Grain size in microns, versus average Hg concentrations for the experiments A001, A002, and B001. B001 has lost virtually all mercury upon melting. X-axis refers to the grid sizes used to physically separate the different particles. b) Mass (mg) input in the analyser against the average Hg concentration averages for the same samples. A001 and B001 could only be measured once per grain-size fraction group.

The concentration values were averaged per increments of 0.5 mg of mass, regardless of grain size. Vertical error bars stand for the standard deviation of the concentration averages in a) and b), and horizontal error bars in b) stand for the standard deviation of the measured masses. The incoherence between the trends and A001 and A002 seems to be related to grain size rather than mass (see labels in A001 for grain size), however, within A001, there is an increase in concentration at masses < 3 mg.

2.4. Summary.

We tested two different analytical techniques for the measurement of Hg in our experiments: LA-ICP-MS, and direct mercury analysis through AAS with thermal decomposition (Lumex RA-915+ multifunctional mercury analyser).

While LA-ICP-MS showed promising results (Figure 2. a & b) for the measurement of Hg concentrations over 100 ppm, it did not perform as well when presented with smaller concentrations. This might be mainly due to Hg having seven stable isotopes, which significantly reduces the amount of Hg that can be detected per isotope and that cannot be distinguished from the background signal. As the Hg concentration in natural basalts is several orders of magnitude lower than 100 ppm (~10 ppb Hg, Canil *et al.,* 2014; Coufalik *et al.,* 2018), the LA-ICP-MS is too limiting for our interest.

The Lumex direct mercury analyser, on the other hand, was accurate down to a few ppb and provided consistent results for the measured basalt standards. Due to the logistic and analytical advantages of the Lumex device (section 2.2. Assessment of Lumex RA-915+ multifunctional mercury analyser.), we carried out all our total mercury analyses in silicate glasses using this technique.

Ultimately, we tried to improve our total mercury concentration measurements when using the Lumex analyser by looking for the ideal grain size and mass input for mercury release during combustion. Based on our limited data (Figure 3. a) and the literature (e.g., Fostier & Melendez-Perez 2013), we set the ideal grain size at under 354 microns.

Chapter 3. Volatility experiments.

In this chapter, we describe all the different attempts at keeping mercury in silicate glass after high-temperature melting. The different compositions are named IBC0, IBC1, etc., and are made by mixing different concentrations of Hg in the form of HgO and a number of other trace elements as oxides into Icelandic Basalt rock powder (Table 1). The glasses are named after the apparatus used and the run number 'n': B00n for box furnace runs, and A00n for piston-cylinder press runs (Table 2). The suffix "IBTS" will indicate Icelandic Basalt Time Series, and 2 digits will be appended to indicate the runtime in minutes (Table 2).

Table 1. Summary of all compositions and the experiments in which they were used.

Composi-tion	Mercury concentra-tion (ppm)	Other elements	Sulfide	Experiments
IBC0	9742.33			A000
IBC1	9981.98	Tl, Ag, Ge, Se, Sb, and Cd		B001
IBC2	1023.17	Tl, Ag, Ge, Se, Sb, and Cd		A001, A002
IBC3	999.00	Tl		A003, A004, A005
IBC4	999.00	Tl	FeS	A006*, A007*, A008, A009
IBC4+HgS	87100.00	Tl	FeS, HgS	A011
IBC5	86000.00	Tl	HgS	A010

IBC8	0	Tl, Ag, Ge, Se, Sb, Cd, Cu, Ga, In, Pb, Zn, Cr, V, and Co	FeS	A012, A013

* Indicates failed experiments.

Table 2. List of Hg concentrations measured with Lumex in the silicate for all Hg-bearing samples produced in this project.

Name	Hg concentration (ppm)	*σ(n)*	Hg loss (%)	Sleeve	Time (min)	Pressure (GPa)	Temperature (ºC)
A000	85.4	0.035(3)	99.99	CaF_2	10	1.5	1450
B001	36.2	14.5	99.99	No sleeve	3	1 atm	1300
A001 _250	128	(1)		CaF_2	60	1.5	1375
A001_354	46.2	(1)	93.2693	CaF_2	60	1.5	1375
A001_500	32.4	(1)		CaF_2	60	1.5	1375
A002_125	243.6	70.14(4)		CaF2	30	1.5	1375
A002_250	214.3	41.33(3)	76.7391	CaF2	30	1.5	1375
A002_354	283.5	52.50(2)		CaF_2	30	1.5	1375
A002_500	149.5	1.50(2)		CaF_2	30	1.5	1375
IBTS60	0.118	0.06(2)	99.99	NaCl+Pyrex	60	1.5	1425
IBTS30	0.566	0.16(2)	99.98	NaCl+Pyrex	30	1.5	1425
IBTS10	0.257	0.18(2)	99.96	NaCl+Pyrex	10	1.5	1425
IBFeS10	0.010	(1)	99.99	NaCl+Pyrex	10	1.5	1425
IBFeS40	0.373	(1)	99.99	NaCl+Pyrex	40	1.5	1425
IBFeSHgS20	134	37.65(4)	99.96	NaCl+Pyrex	20	1.5	1425
NiC1	1.22	(1)	99.99	CaF_2	60	1	1200
NiC2	41.20	(1)	99.99	CaF_2	60	1	1200

σ – Standard deviation

n – number of measurements

3.1. Methods.

3.1.1. Preliminary experiments: Glasses A001, A002 and B001.

To find a potential correlation in the geochemical behaviour of Hg and other chalcophile elements, we added Hg and chalcophile trace-elements to the same Icelandic basalt powder, in the form of analytical grade oxides (Tl_2O_3, Ag_2O, GeO_2, SeO, Sb_2O_3, and CdO), at 1000 ppm concentration to create the mixtures "IBC1" and "IBC2" (Table 2), and added 1 wt % HgO to IBC1, and 1,000 ppm HgO to IBC2. The additional elements were chosen for their chemical similarity to Hg (affinity to sulfur, high volatility, and even similar atomic number in the case of Tl), to explore similarities in their behaviour. Each of the mixtures was ground with ethanol four times to ensure homogenisation. IBC1 was melted at 1 atm and 1300ºC for 3 minutes in an alumina crucible (glass B001, Table 2), whereas IBC2 was used as the starting material for two piston-cylinder press experiments at 1.5 GPa and 1375ºC: A001 (1h) and A002 (30 minutes) (See Table 2).

For both A001 and A002, the rock powder mixture was loaded into a 6 mm diameter graphite capsule and dried overnight at 110ºC. The Pt capsule used in the trial experiment most likely served as a sink for mercury, as it has been shown that it can be absorbed into the structure of platinum at temperatures above 150^{o}C (Fertonati *et al.*, 1999: Granite & Pennline 2006) and the Hg loss for this experiment was over 99% (Table *2*). To clarify this process, a different experiment should be run at a range of temperatures with a HgO-only powder loaded Pt capsule, and the

concentration of this element measured with LA-ICP-MS. We did not undertake this within this project.

To prevent the undesirable dissolution of Hg into the Pt structure, we used a graphite capsule in all the subsequent experiments. Albeit this approach had the downside that it could not be completely sealed.

The experimental cell consisted of a graphite furnace packed with MgO pieces and surrounded by a thick CaF_2 sleeve (Figure 1. b). Additionally, A002 also included two Fe_2O_3 pressed discs on the top and bottom of the graphite capsule with the goal of maximizing the anhydrous character of the experiment (Figure 1. c). The A001 glass was mounted in acrylic, polished down to 1 µm, and carbon-coated for SEM (Scanning Electron Microscopy) imaging.

3.2.1. Second batch of experiments: Silicate time series or "IBTS".

We carried out another series of experiments to parameterise the potential effect of run time on the evaporation of Hg from the glass. The run lengths were 1 h (A003, IBTS60), 30 min. (A004, IBTS30), and 10 min. (A005, IBTS10) (See Table 2).

We attempted to improve the methodology applied in section 3.1.1. by correcting the issues arisen with A001 and A002. Because we observed with SEM the formation of metallic phases containing Hg, Ag, Sb, Ni, Se, and Tl in the A001 glass, the new Icelandic basalt mixture contained only 1000 ppm of Tl and Hg each (IBC3, Table 1). This powder was prepared as described in the previous section, loaded in 6 mm graphite capsules, and dried overnight at 110ºC.

I ran all experiments at 1.5 GPa. To reduce the risk of formation of metallic phases in the glasses, we increased the run temperature to 1425ºC. The sample cell was also modified to optimise the transmission of pressure: the CaF_2 was replaced by a 12.5 mm O.D. and 10 mm I.D. NaCl outer sleeve and a pyrex 8 mm I.D. tube as an inner sleeve (Figure 1. d). The salt sleeves were manufactured from reagent-grade NaCl powder that had been kept at room temperature to preserve some of the moisture. NaCl requires a very low friction correction (3%, McDade *et al.*, 2002), while the Pyrex insulator provides a separation layer between the salt and the graphite heater, to prevent the potential intrusion of the salt in the core of the sample cell. However, it is also unstable at high pressures, melting at just above 1000ºC at 1.5 GPa (Akella *et al.,* 1969), and therefore, all the experiments presented shearing parallel to the compression and NaCl intrusion in the furnace. However, all the capsules remained intact.

The resulting glasses were ground into fine powder under 354 µm with an agate mortar and sieved for homogeneity.

3.2. Analysis, results, and discussion.

Experiment A001 presented metallic and silicate phases which were observed with reflected microscopy and later characterised with SEM. The metallic phases contained variable amounts of Hg, Ag, Sb, Ni, Se, and Tl, while the silicate phases were olivine. No other glasses presented metallic phases and therefore no further analysis of this kind was conducted.

Both A001 and A002 Hg concentrations were determined with the Lumex RA-915 mercury analyser. The standards used for the calibration were NIST 1944 New Jersey Waterway sediment (3.4 ppm Hg) and 2782 Industrial sludge (1.1 ppm Hg) and the BCR's BR 45.5 (45.5 ppm Hg). When compared against their initial concentrations, the mercury loss was 93.27 % and 76.74 % for A001 and A002 (Table 2) respectively. The effect of grain size has already been discussed in chapter 2, section 2.3, and established to be optimal for our measurements when this is < 354 µm.

To analyse the time series, we used the NIST reference standard SRM 2587 Trace Elements in soil containing lead from paint (290 ppb), and the basalts BR —45.5 and BE-N— 12 for our calibrations and an input mass between 9 and 19 mg of synthetic silicate glass powder per measurement. Due to the limited size of the samples, our data points were just a couple per glass, all obtained Hg concentrations ranged between 0 ppb and 726 ppb, with no consistent values obtained between measurements of the same experiment (e.g., IBTS10 recorded 74 ppb and 441 ppb, table 2) or across the series (Figure 4). On top of this, the mercury loss for all samples was > 99.96% (Table 2).

In addition to this, there is no clear pattern shown of mercury loss in function of time and since the variance between measurements is so significant, the regressions are not reliable (R^2 ~ 0.16, Figure 4).

With these experiments, we show that the high volatility of Hg is a great drawback when carrying out experiments at high temperatures. However, we cannot predict future losses from the evaporation of mercury since the results obtained were not consistent enough to establish a reliable relationship between the different experimental conditions and the Hg loss to evaporation.

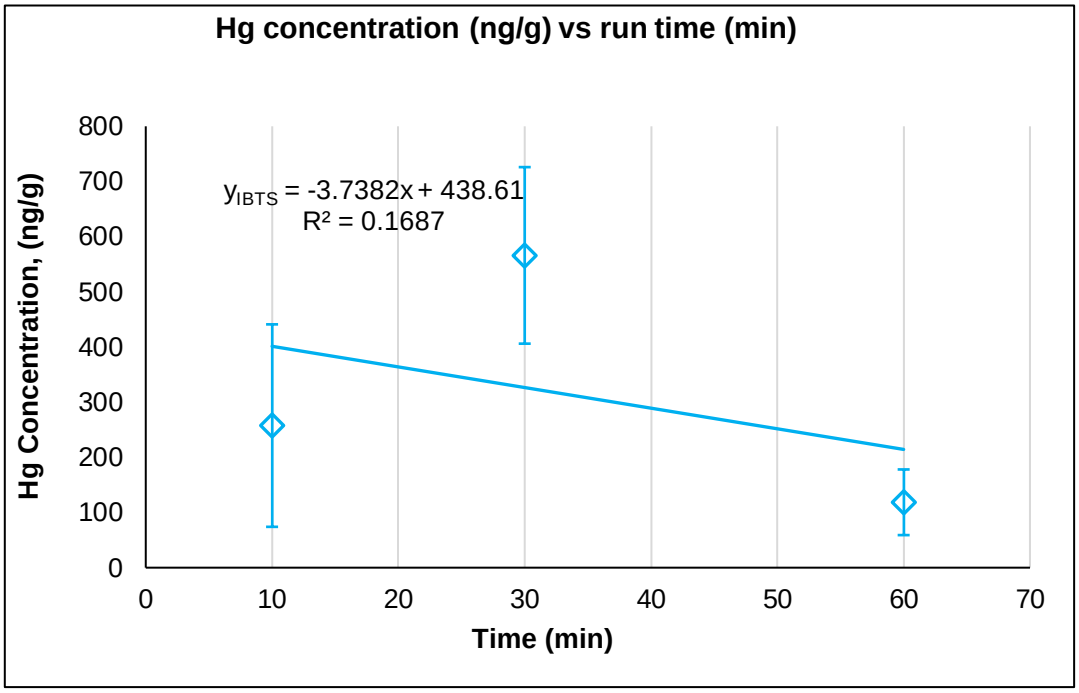

Figure 4. Average Total Hg concentrations of IBTS glasses in function of the duration of the experiment. Vertical error bars correspond to the standard deviation. The plot shows that Hg is almost completely lost during the heating process.

Using a low friction support medium like NaCl and pyrex did not improve the retention of Hg for the IBTS series. In fact, the experiments A001 and A002, which were produced with a CaF_2 thick sleeve, at a lower temperature than the IBTS ones, presented the smallest Hg loss (Table 2). Nevertheless, the use of an unwelded and permeable graphite capsule seems to contribute to the loss of Hg. A metallic, welded capsule might prevent this, but this will be another challenge to solve, due to the

predisposition of Hg to form alloys with virtually all metals except for iron —which would make it harder to control the redox conditions of the experiment.

3.3. Summary and further thoughts.

We performed piston-cylinder experiments on HgO-bearing Icelandic basalt rock powder mixtures. The first attempt included a mix of trace-elements that produced a heterogeneous glass with metallic inclusions, which is undesirable and can be avoided in future experiments by removing elements that might form such heterogeneities in the glass.

We conducted the experiments with two kinds of sample assembly: one supported by a thick CaF_2 sleeve (A001 and A002, figure 1. b & c), and another one supported by a NaCl thin sleeve and a borosilicate glass tube insulator (IBTS, figure 1. d). The latter was used with the objective of maximising the transmission of pressure into the capsule. A graphite capsule was used in all the runs, as opposed to the Pt capsule used for the A000 trial experiment, so that potential loss of Hg to the capsule was prevented.

While all silicate glassed presented major loss of Hg (>93 %, Table 2), the A002 experiment retained the most mercury —~23% over the initial input of 1000 ppm. This glass was synthesized at 1375^{o} C and 1.5 GPa, for 30 minutes. Additionally,

the A002 sample cell was the only one that had Fe_2O_3 on the top and bottom of the capsule.

The IBTS time series preserved very small amounts of Hg and did not show any trend relating to runtime (Figure 3).

All in all, it is clear that for the range of experimental conditions explored, Hg tends to be almost completely lost to evaporation, and using a ‘frictionless’ sample-cell to increase the transmission of pressure does not improve the retention. Nonetheless, A002 might open a more promising path to reducing the loss of Hg at high temperature, and therefore more experiments should be conducted replicating the described sample-cell.

Chapter 4: Sulfide-silicate partitioning experiments.

The following section describes the experimental methodology used to study the distribution of 14 trace elements of diverse geochemical nature, in a sulfide-silicate system at equilibrium for a range of pressures from 0.5 GPa to 2 GPa. These samples will be referred to as “SSP suite”, that is, “Sulfide-Silicate Partitioning suite”.

4.1. Sulfide-silicate partitioning model: theoretical background.

The experiments are an extension of the sulfide-silicate partitioning model developed by Kiseeva & Wood (2013), which establishes that the tendency of chalcophile elements to partition into the silicate phase is linearly dependent on the FeO concentration in the silicate melt when the phases at equilibrium are sulfide-rich liquids and anhydrous mafic melts.

Since the concentration of FeO in the silicate melt is heavily related to the content of available oxygen in the system, this model uses the concentration of FeO as a proxy for oxygen fugacity to estimate the sulfide-silicate partition — or distribution — coefficient, $D_M^{Sulf/Sil}$, for a given element M with a valence n. Typically, the exchange reaction of M between two immiscible sulfide and silicate liquids is expressed in terms of oxygen and sulfur,

$$MO_{\frac{n}{2}} + \frac{n}{4}S_2 = MS_{\frac{n}{2}} + \frac{n}{4}O_2 \qquad \text{(eq. 2)}$$

$silicate\ sulfide \quad sulfide\ silicate$

Nevertheless, if we express the partitioning reaction terms of Fe species as stated by Kiseeva & Wood (2013),

$$MO_{\frac{n}{2}} + \frac{n}{2}FeS \;\; = \;\; MS_{\frac{n}{2}} + \frac{n}{2}FeO \qquad \text{(eq. 3)}$$

$silicate\ sulfide \quad sulfide\ silicate$

the partition coefficient can be expressed as follows:

$$log\left(D_M^{Sulf/Sil}\right) \approx A + \frac{n}{2} log[FeO]_{silicate} \qquad \text{(eq. 4)}$$

Here, A is a constant related to the free energy of the $Fe_{\ sulfide} - M_{silicate}$ exchange reaction, n is a constant related to the valence of the element ($n \sim -1$ for $+1$ ions, $n \sim -2$ for $+2$ ions, etc.), and $[FeO]_{silicate}$ is the FeO content in the silicate, expressed in wt% or mol %.

If we express the partitioning process in terms of the exchange reaction $Fe_{\ sulfide} - M_{silicate}$ as in equation 2, the ratio $f_{S_2}^{sulf}/f_{O_2}^{sil}$ that would be otherwise required to estimate $D_M^{Sulf/Sil}$ can be easily approximated to the ratio of the activity of FeS in the sulfide liquid to the activity of FeO in the silicate melt.

This relationship is only valid provided the sulfide liquid is almost entirely FeS and at equilibrium with the silicate melt, at high pressure and temperature. The approach simplifies the prediction of the partitioning behaviour of many trace elements, as it solely depends on the measurement of FeO concentration, $[FeO]$, in the silicate

(Kiseeva & Wood 2013). If the sulfide liquid were to consist of different sulfide species with variable amounts of Fe, Ni and Cu (in a FeS—NiS—$CuS_{0.5}$ sulfide liquid), $[\mathrm{FeO}]$ should be adjusted to $[\mathrm{FeO}]_{corrected}$ by the following expression (Kiseeva & Wood 2013; 2015),

$$[\mathrm{FeO}]_{corrected} = \frac{[\mathrm{FeO}]_{silicate}}{[\mathrm{Fe}/(\mathrm{Fe+Ni+Cu})]_{sulfide}} \quad \text{(eq. 5)}$$

The model was expanded in Kiseeva & Wood (2015) to account for the effect of temperature, as well as the effect of the sulfide composition (FeS—NiS—$CuS_{0.5}$—FeO).

$$log\left(D_M^{Sulf/Sil}\right) = A + \frac{B}{T} - \frac{n}{2} log[FeO]_{corr} + \frac{1673}{T}\left[\varepsilon_{MS_{\frac{n}{2}}}^{FeO}\, log(1 - x_{FeO}) + \varepsilon_{MS_{\frac{n}{2}}}^{NiS}\, log(1 - x_{NiS}) + \varepsilon_{MS_{\frac{n}{2}}}^{CuS}\, log\left(1 - x_{CuS_{0.5}}\right)\right] \quad \text{(eq. 6)}$$

Where B is a constant related to the enthalpy of the $Fe - M$ exchange reaction where M is the element of interest, x_i are the mole fractions of the respective compounds in the sulfide, and n is again the valence of the element of interest. This expression introduces the "interaction parameters," $\varepsilon_{MS_{\frac{n}{2}}}^{i}$, where i equals FeO, NiS, and $CuS_{0.5}$, based on the epsilon model described in Ma (2001). These parameters represent the non-ideal interactions between the given trace element M and individual components of the sulfide solvent.

This model was tested for the following elements Ag, Cd, Co, Cr, Cu, Ga, Ge, In, Mn, Ni, Pb, Sb, Ti, Tl, V and Zn, and demonstrated that temperature affects these element's distribution into the sulfide liquid negatively (Ag, Ni, Cu), positively (Ga, Ge, Cr, V, and Ti), or not at all (Co, Cd, In, Mn, Pb, Tl, and Zn) (Kiseeva & Wood 2015).

While the effect of pressure might be subordinate to the effect of temperature (Li & Agee 1996), this should not be assumed without proper empirical confirmation, therefore, this chapter addresses this gap of knowledge by testing the elements Ag, Cd, Co, Cr, Cu, Ga, Ge, In, Pb, Se, Sb, Tl, V, and Zn at pressures ranging from 0.5 GPa to 2 GPa.

4.2. Methods.

4.2.1. Sulfide-Silicate partitioning experiments (SSP suite).

I prepared a mixture consisting of ~50:50 FeS and synthetic silicate. The silicate constituent was Icelandic basalt (Norris 2016). The basaltic powder was ground and doped with a mixture of trace-elements, containing Ag, Cd, Co, Cr, Cu, Ga, Ge, In, Pb, Se, Sb, Tl, V, and Zn as oxides, with the exception of Se which was added as a native element, to make up to ~2 wt. % of the silicate (~1500 ppm each). FeS was added to the mixture in the following step, and ground with ethanol, to achieve homogeneity.

The mixture was packed in a 3 mm outside diameter (O.D.) and 1 mm inside diameter (I.D.) graphite capsule. The capsule was protected by a tight MgO ring (4 mm O.D. and 3 mm I.D, 4.25 mm height). A ~0.5 thin alumina disk was placed on top of the ring and supported by crushable MgO pieces filling the graphite furnace as described in chapter 3 (Figure 1. h.). The pressure medium used was a 32 mm long CaF_2 sleeve, 8 mm I.D., and 4.5 mm wall thickness. For more details describing the manufacturing of the pieces and set-up of the thermocouple, refer to chapter 2. The low-pressure experiments (0.5-0.8 GPa) used a thin 12.5 mm O.D. and 10 mm I.D. NaCl outer sleeve and a pyrex 8 mm I.D. tube as an inner sleeve, to improve the pressure transmission (see chapter 3, 3.2). Experiments were performed in an end-loaded Boyd–England-type piston-cylinder apparatus (Boyd & England 1960) at the University of Oxford. We tested 0.5, 0.8, 1, 1.5, and 2 GPa using the pressure calibrations of McDade *et al.* (2002) for ≥1 GPa, and Vlach *et al.* (2019) for <1 GPa, for a 1300^{o} C-1500^{o} C temperature range (Table. 3). The experiments performed under 1 GPa had an additional continuous Ar supply to prevent oxygen flow through the thermocouple, since the low pressure may not deform the assembly enough to seal the plug around the thermocouple. I used a steel plug instead of the brass plug that is used at higher pressures to prevent the oxidation of the thermocouple wire.

For all experiments, temperature and pressure were increased manually at a rate of 150-200°C/min, and 50-100 p.s.i./min respectively. The pressure gauge has a minimum subdivision of 20 p.s.i. (~0.14 MPa) which provides a range of ±10 p.s.i. uncertainty over the set pressure. The experiments were run at the chosen conditions for a duration of 1 h. Former studies (Tuff *et al.,* 2011; Kiseeva & Wood

2013; Kiseeva & Wood 2015; Smythe *et al.,* 2017; Streenstra *et al.,* 2018; Streenstra *et al.,* 2020) state that such duration exceeds the minimum time required to achieve sulfide-silicate partitioning equilibria for the temperature conditions explored in this study. We quenched the experiments by cutting off the power at the run pressure, cooling at a rate of ~60-40°C/s. The pressure was slowly released once the samples reached a temperature below 40°C.

Table. 3. List of analysed samples belonging to the SSP-suite and NiC experiments* and the experimental conditions under which they were produced.

Run No.	Starting composition	Duration (h)	T (°C)	P (GPa)	Capsule	Sleeve
SSP13-1	IB+FeS	1	1300	1	Graphite	CaF2
SSP14-1	IB+FeS	1	1400	1	Graphite	CaF2
SSP15-1	IB+FeS	1	1500	1	Graphite	CaF2
SSP14-1.5	IB+FeS	1	1400	1.5	Graphite	CaF2
SSP14-2	IB+FeS	1	1400	2	Graphite	CaF2
SSP15-2	IB+FeS	1	1500	2	Graphite	CaF2
NiC1	FeS+ 5% HgS	1	1200	1	Ni+Graphite	CaF2
NiC2	FeS+ 5% HgS	1	1200	1	Ni+Graphite	CaF2

*See chapter 5, 5.3

The capsules were mounted in epoxy resin and hand-polished down to 1 µm with sandpapers of decreasing grit size and diamond powder. The products presented segregated black silicate glasses and metallic grey sulfide regions, with some sulfide spherules within the glass section (Figure 5.).

All the experiments performed under 1 GPa were unsuccessful; the material escaped from the graphite partially or completely. Additionally, some experiments that were performed at pressures ≥1 GPa contained too little sulfide area to be analysed, potentially due to material loss from the capsule. This is likely due to the loose packing of the sample cell, or the capsule not fitting tightly enough inside the MgO ring. These issues were corrected in the subsequent experiments by modifying the pieces manually to fit as tightly as possible, but those under 1 GPa continued to partially leak. The graphite material used in the capsule was the same used in Kiseeva & Wood (2013), where it is reported to seldom present cracking (Kiseeva & Wood 2013, supplementary material), while the experiments carried out in this study show evidence of fissures (Figure 6). There is a possibility that those fractures occurred during decompression and cooling of the capsule, however, the material loss during the low-pressure experiments point out that the capsule did not seal completely. Moore *et al.* (2008) addressed the issue regarding the ineffective “seal” of the thermocouple wire at pressures below 0.5 GPa, due to insufficient deformation at low pressure and temperatures prior to heating. This may also have occurred for the pieces surrounding the capsule in the low-pressure runs in this study. The already weaker —compared to a welded capsule— seal of the graphite capsule might have fitted poorly, allowing the material to migrate.

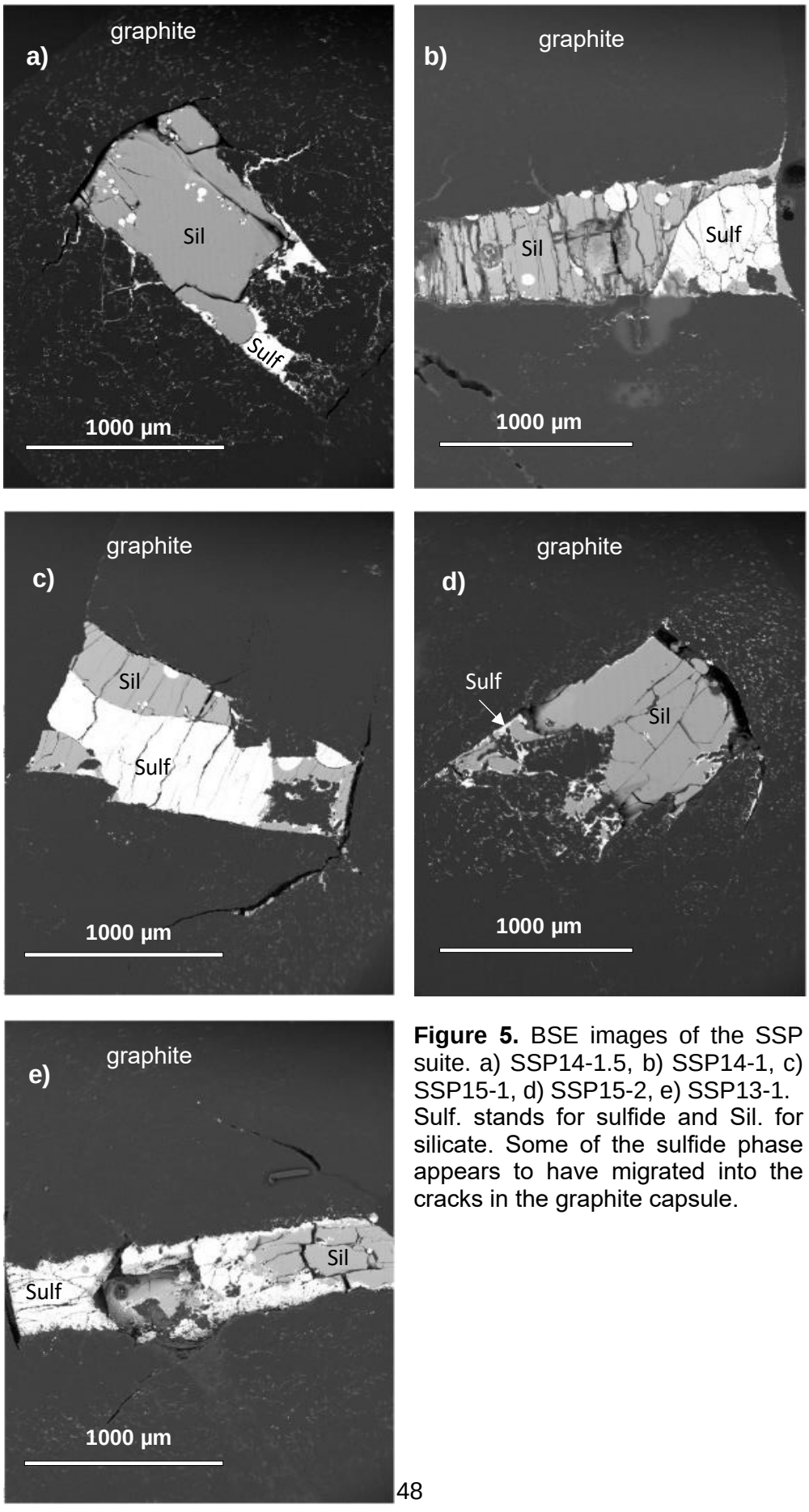

Figure 5. BSE images of the SSP suite. a) SSP14-1.5, b) SSP14-1, c) SSP15-1, d) SSP15-2, e) SSP13-1. Sulf. stands for sulfide and Sil. for silicate. Some of the sulfide phase appears to have migrated into the cracks in the graphite capsule.

We attempted to improve this issue by first inverting the capsule position so that the risk of creating fractures on the lid of the capsule was minimised, but the results did not improve significantly since the material was mostly gone after quenching. We attempted to improve this issue by first inverting the capsule position so that the risk of creating fractures on the lid of the capsule was minimised, but the results did not improve significantly since the material was mostly gone after quenching.

The assembly for these experiments has already been successfully used for the pressure and temperature range intended (Kiseeva & Wood 2013; 2015; Prof. Wood's personal communication). The discussion of how to improve these complications is further developed below (section 4.3.1.).

4.3. Analysis, results, and discussion.

4.3.1. Major element analysis.

A) Silicate glass.

The resulting successful glasses and sulfides for the SSP suite, the sulfide-bearing time-series, and the double-capsule experiments, were analysed on the CAMECA SX-5-FE at the University of Oxford's Department of Earth Sciences and the JEOL-8600 at the University of Oxford. For the silicate analysis (SSP-suite only), we performed Wavelength-dispersive X-ray spectroscopy (WDS) point analyses with a 40-41 nA beam current, 15 kV accelerating voltage, and a defocused 10 µm spot size. The standards selected for the calibration were Albite (Na, Si, Al), MgO (Mg), Sanidine (K), TiO_2 (Ti), native Mn metal (Mn), Andradite (Fe, Ca), Pyrite (S). The peak times used for every element were 20 s for Na and K, 30 s for Si, Al, Mn, Fe,

S, and Ca 35 s for Mg and Ti. The spots were collected from clear glass surfaces, avoiding neighbouring cracks and borders, and the size of the sample population was limited to ~10 spots per glass, due to time constraints.

All silicate glasses that were produced using a CaF_2 sleeve, except for those made at 2 GPa, present low totals (Table 4), indicating the presence of other elements in the glass not included in the analytical routine. The missing element was shown to be F through Energy-dispersive X-ray spectroscopy (EDS). The results are relatively homogeneous for most elements with low standard deviations, however, SiO_2 and CaO are inconsistent in all glasses but SSP14-2 and SSP15-2. The composition obtained for these glasses is moderately poorer in almost all elements compared to the starting material, particularly SiO_2 with a relative difference of -4.34 % to -35.85 %. On the other hand, CaO experienced substantial relative enrichment (from 27.19 % to 200.73 %) in all glasses except for SSP14-2 and SSP15-2. MgO is also high in the samples SSP14-1 (+64.78 %) and SSP14-1.5 (+12.21 %). FeO values present moderate variation throughout all the glasses. The most likely source for this contamination is the sample cell's sleeve (CaF_2) and the spacing pieces (MgO).

While there is no specific documentation on contamination of the capsule from the supporting pieces (sleeve and spacers) of the assembly, there are a few examples of contamination into the capsule and the thermocouple from other structural pieces of the sample cell. Brooker *et al.* (1998) mention contamination from the graphite furnace into the capsule at high temperature and high pressures, Moore *et al.* (2008), dealt with contamination from the furnace, which is corrected by using a

double metallic capsule (an Au80-Pd20 alloy inner capsule surrounded by a Pt capsule).

Kiseeva & Wood (2013; 2015) encountered no contamination issues while using the same cell assembly for pressures equal to 1.5 GPa and over. The SSP experiments in this study replicate the same cell assembly, however, since there are clear issues of contamination, these issues are more likely due to small inaccuracies when custom-fitting the pieces of the assembly, as well as choosing too low of a starting sample pressure for the lower pressure runs. At high temperature, the lower the pressure, the higher the potential for thermal expansion of the materials, which can generate displacement of the different pieces as temperatures rise, resulting in ineffective sealing of the capsule. This issue is evident in the experiments performed at ≤1 GPa since, after decompression, the lid would separate from the capsule body. The thermal expansion may easily be counteracted by increasing the starting sample pressure, prior to raising the temperature —the experiments ran at 0.5-1.5 GPa in this study and were initially pressurized to 150-250 p.s.i. gauge pressure. Both issues should be straightforward to fix in future experiments.

With those adjustments, the experiments performed at 0.5 GPa might still be problematic as the target pressure is very low. If they are, we would suggest attempting to implement crushed Pyrex and MgO pieces, as spacers, together with a NaCl and Pyrex sleeve

Table 4. Major elements of the silicate glass for the SSP suite, percentage by mass.

Run No.	SSP13-1	σ	SSP14-1	σ	SSP15-1	σ
n	11		10		10	
SiO_2	42.07	0.60	44.34	0.37	33.68	0.17
TiO_2	0.74	0.02	0.79	0.02	0.60	0.01
Al_2O_3	11.68	0.34	13.05	0.15	9.72	0.04
FeO	9.99	0.34	6.92	0.09	1.71	0.50
MgO	9.28	0.16	14.93	0.29	9.05	0.11
CaO	19.73	0.71	15.67	0.21	37.05	0.21
MnO	0.10	0.01	0.09	0.01	0.06	0.01
Na_2O	1.34	0.07	1.69	0.04	0.84	0.01
K_2O	0.05	0.01	0.05	0.01	0.03	0.01
S	0.20	0.01	0.27	0.01	0.33	0.13
Total	95.17	0.37	97.81	0.24	93.07	0.22

n – No. of measurements. σ - Standard deviation.

The borosilicate glass and NaCl sleeve combinations have been used successfully for experiments under 0.5 GPa by Moore *et al.* (2008) and Vach *et al.* (2019) since the effect of friction is significantly reduced in this kind of set-up, and thus pressure is more effectively transmitted to the capsule (McDade *et al.*, 2002).

Still, there is a risk of contamination from borosilicate, due to the increased chance of volatilization of Cs from the glass at temperatures over 950^{o} C (Banerjee *et. al.,* 2012). If this modification does not resolve the issue, we would suggest moving the range of pressures for this suite of experiments to higher and more stable pressures.

Table 5. (continuation) Major elements of the silicate glass for the SSP suite, percentage by mass.

Run No.	SSP14-1.5	σ	SSP14-2	σ	SSP15-2	σ
n	9		10		10	
SiO_2	32.41	0.33	47.49	0.24	48.33	0.16
TiO_2	0.60	0.02	0.86	0.02	0.87	0.02
Al_2O_3	9.23	0.14	13.58	0.08	14.02	0.06
FeO	7.43	0.24	10.93	0.05	10.97	0.06
MgO	10.17	0.05	9.28	0.13	9.03	0.05
CaO	30.73	0.42	12.96	0.28	12.20	0.03
MnO	0.07	0.01	0.12	0.01	0.13	0.01
Na_2O	0.98	0.02	1.83	0.07	1.88	0.02
K_2O	0.03	0.01	0.06	0.01	0.06	0.01
S	0.26	0.09	0.17	0.00	0.24	0.01
Total	91.89	0.21	97.28	0.19	97.72	0.14

n – No. of measurements. σ - Standard deviation.

B) Sulfide phases.

We also obtained the major elements in the sulfides through WDS point analysis for the SSP suite. The IBFeS time series was analysed at 15 kV and ~40 nA beam current. Since the availability of a clean sulfide surface without cracks in the SSP experiment suite was scarce, we used a defocused 5 µm spot size. The standards used were pyrite (Fe, S), MgO (O), and cinnabar (Hg). The peak counting times were 30 s for Fe and Hg, 45 s for S, and 60 s for O. The sulfides SSP13-1sf, SSP14-1.5sf, and SSP15-2sf were analysed without considering Hg. The number of spots measured for the SSP sulfides was again, ~10, due to the lack of clean surfaces.

For the SSP suite the standard deviations for all elements are generally high (σ >1), which indicates heterogeneity within the sulfides (Table 6). However, the calculated average for each element is relatively consistent across different experiments.

Table 6. Major elements of the sulfides, and Hg, in wt.%

Run No.	SSP13 -1sf	σ	SSP15 -1sf	σ	SSP14 -1.5sf	σ	SSP14 -2sf	σ	SSP15 -2sf	σ
n	9.00		11.00		12.00		10.00		8.00	
O	1.99	1.33	0.58	0.15	2.55	1.60	3.09	3.24	1.49	0.93
Ni	n.m.		n.m.		n.m.		n.m.		n.m.	
S	35.45	1.55	30.89	1.67	33.41	3.65	34.59	3.67	35.99	0.97
Fe	62.96	0.26	68.62	1.72	62.50	4.84	60.25	6.22	62.62	0.41
Hg	n.m.		n.m.		b.d.l		b.d.l		n.m.	
Total	100.40	0.43	100.09	0.42	98.74	8.14	98.07	6.97	100.10	0.57

n.m. - not measured. b.d.l. – below detection limits

4.3.2. Minor element analysis.

Contamination-free SSP14-2 and SSP15-2 were analysed with LA-ICP-MS to calculate sulfide-silicate partition coefficients. All LA-ICP-MS trace-element measurements were performed with a quadrupole-based Perkin Elmer Nexion mass spectrometer coupled to a New Wave Research UP213 Nd: YAG laser at the

University of Oxford. We used NIST 610 and GSE-1G USGS glass standards as our primary and secondary external standards, respectively. The FeO values obtained with the microprobe were used as a reference for both sulfides and silicates. The isotopes measured were: ^{29}Si, ^{33}S, ^{51}V, ^{53}Cr, ^{57}Fe, ^{59}Co, ^{61}Ni, ^{65}Cu, ^{66}Zn, ^{71}Ga, ^{74}Ge, ^{77}Se, ^{107}Ag, ^{111}Cd, ^{121}Sb. All phases were measured with a 50 µm beam. We collected 10 spots for each phase, with an initial 20-second background determination, followed by a 40 second dwell time, at 10 Hz. Every ablation was followed by a 60-second washout to transport the aerosol out of the ablation cell. The standards were analyzed systematically every 10 collections to correct sensitivity drift (Liu *et al.*, 2013 and references therein). The masses were collected in counts per second and the peaks adjusted manually for optimization of the results with the GLITTER (www.es.mq.edu.au/gemoc/glitter) software package. The results for elemental iron are coherent with the concentrations obtained with the microprobe, which gives a degree of reliability to the analysis.

The partition sulfide-silicate partition coefficient was calculated for all elements by calculating the ratio between the concentration of the given element in the sulfide over its concentration in the silicate, in ppm.

The distribution of Ag and Cu in the sulfide and silicate melts show a strong negative response to the increase in temperature (Table 7, Figure 5), while the abundance of Ga, Ge, and V in the sulfide experienced a particularly high increment (>40 %). The partition coefficients of Cr, Se, Cd, In, and Pb were moderately affected by the change in temperature (of ~19-30%), and Fe, Co, Zn, Sb, and Tl show only a slight

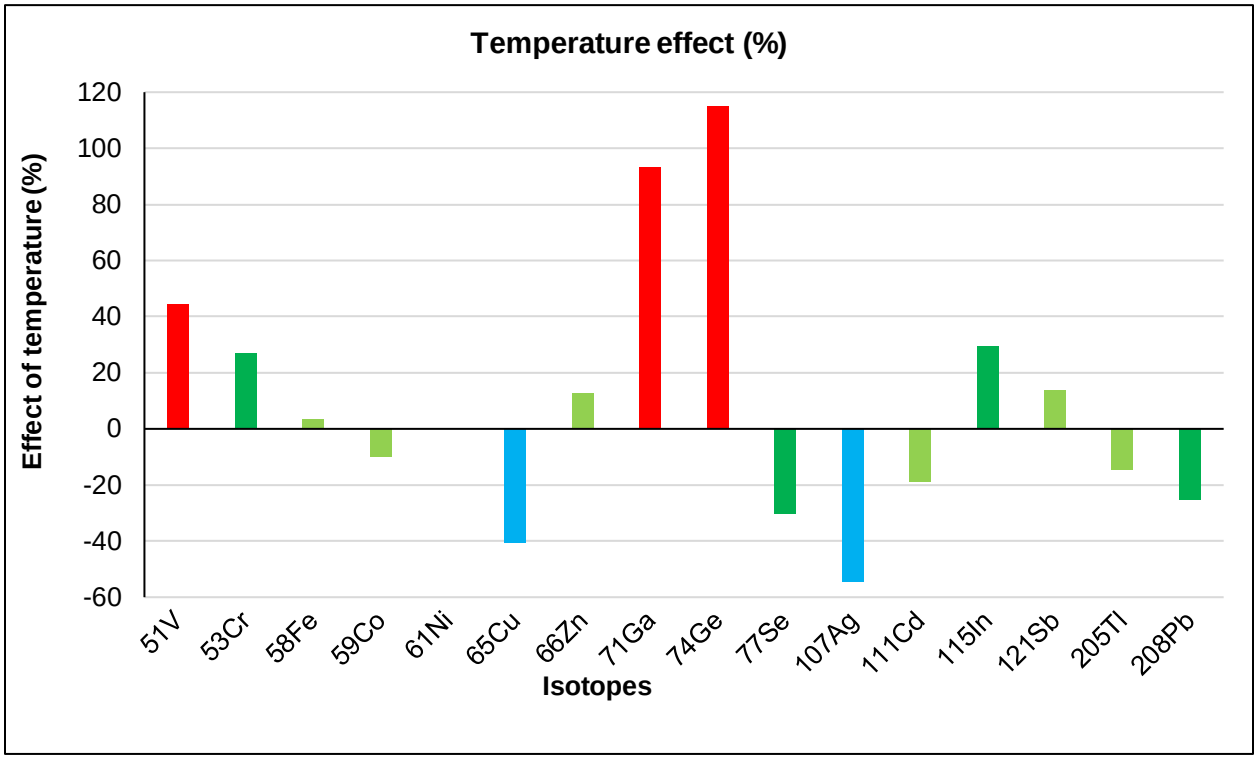

Figure 6. Relative change in temperature for all measured isotopes from 1400° C to 1500° C. Light green shows slight change (<19%), dark green shows moderate change (19-30%), in any direction, red indicates strong increase (>40%), and blue strong decrease (<-40%).

dependency on temperature (-20% > to < 20% difference), and Ni is unaffected by the temperature change.

These observations roughly align with the conclusions on temperature dependency for the different trace elements in Kiseeva & Wood (2015) where the concentrations of Ag, Cu and Ni (more typically chalcophile) decreased significantly with the rise in run temperature, while Ga, Ge, Cr, V and Ti (typically lithophile) tended to distribute more into the sulfide liquid at the same conditions. Co, Cd, In, Mn, Pb, Tl and Zn did not show noticeable sensitivity to the increase in temperature.

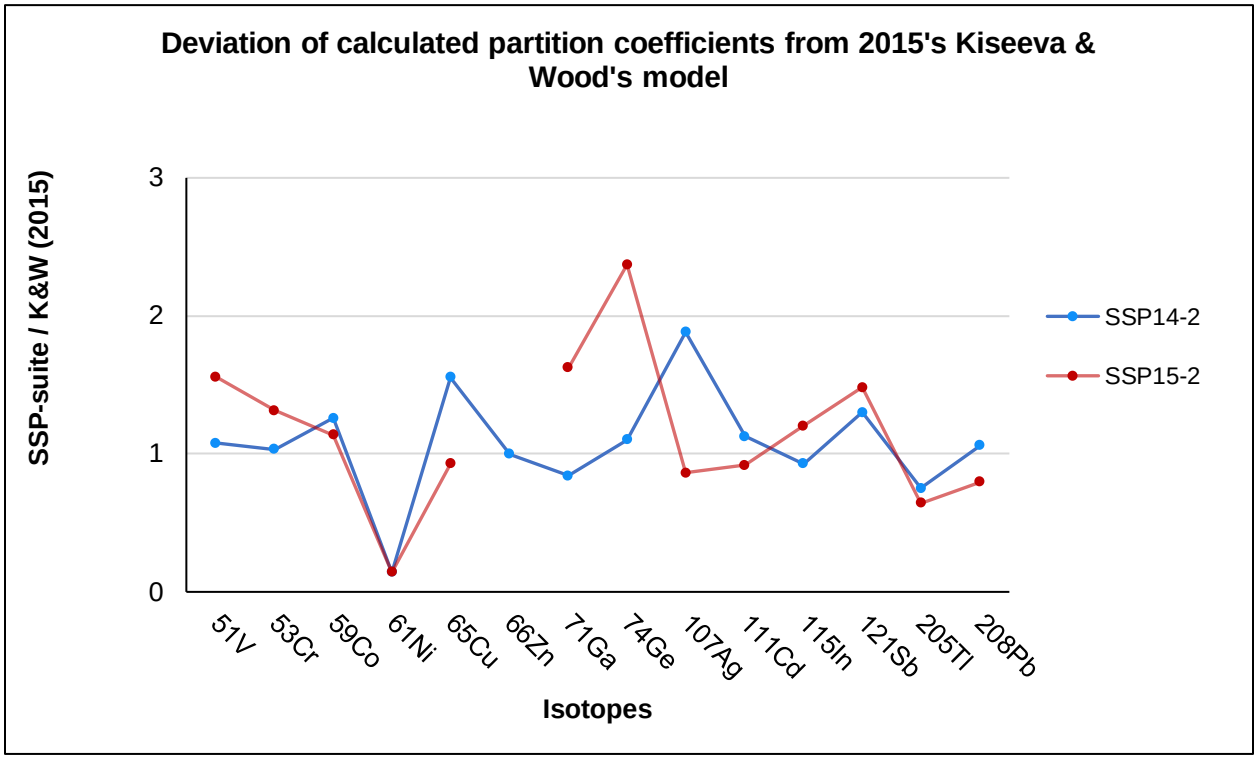

Figure 7. SSP14-2 and SSP15-2 partition coefficients normalized to the partition coefficients calculated by using the spreadsheet calculator in Kiseeva & Wood (2015). ^{66}Zn SSP15-2 was removed because it was 35.63 times greater than the coefficient obtained from the Kiseeva & Wood (2015) model. See text for discussion.

We further input the compositional data and temperature of the glasses SSP14-2 and SSP15-2 into the partition coefficient calculator spreadsheet (Kiseeva & Wood (2015), Appendix A: Supplementary materials). The coefficients obtained in this study were then normalized to the coefficients calculated through the spreadsheet (Figure 7). For most elements, the agreement between both datasets is very high, however $D_{Zn}^{sulf/sil}$ (SSP15-2) deviates strongly from the predictions (Figure 6). Kiseeva & Wood (2015) predicts nearly no change due to the temperature change for Zn, however, we register an increase of 12% in the partition coefficient for that element from the 1400^{o} C to the 1500^{o} C experiment.

While the results in this study correlate with those of Kiseeva & Wood (2015) to a degree, there are a few noticeable differences, such as the invariability of $D_{Ni}^{sulf/sil}$ through the temperature increment and $D_{Zn}^{sulf/sil}$ (SSP15-2) showing a value much higher (Figure 7) than expected. These discrepancies might be due to the higher-pressure conditions (2 Gpa vs the original 1.5 GPa) at which these experiments were carried out. There is evidence in the literature that at pressures up to 45 GPa there is a direct relationship between the increase in pressure and the attenuation of the effect of rising temperature for the Ni-Fe and Co-Fe exchanges (Kegler *et al.,* 2008; Fischer *et al.,* 2015). Even though the attenuation is shown to occur for pressures above 3 GPa (Kegler *et al.,* 2008), these studies report this effect for sulfur-free metal-silicate systems, which do not account for the potential effect that S might have on these reactions. Further experiments at a range of pressures will determine the extent of the effect of pressure on these elements for the given composition.

Table 7. Sulfide-silicate partition coefficients at 2 GPa for the SSP suite.

Element	SSP14-2	SSP15-2	Temperature effect (%)
^{51}V	0.417	0.601	44.35
^{53}Cr	1.966	2.497	26.99
^{57}Fe	56.862	51.267	-9.84
^{59}Co	89.514	89.629	0.13
^{61}Ni	563.085	335.710	-40.38
^{65}Cu	2.108	2.372	12.51
^{66}Zn	0.056	0.108	93.32

^{71}Ga	0.807	1.734	114.95
^{74}Ge	578.870	404.672	-30.09
^{77}Se	862.866	394.426	-54.29
^{107}Ag	60.410	49.111	-18.70
^{111}Cd	10.188	13.200	29.57
^{115}In	22.587	25.722	13.88
^{121}Sb	9.457	8.093	-14.42
^{205}Tl	35.243	26.404	-25.08

4.4. Summary and further thoughts.

I performed a series of experiments replicating the methodology of Kiseeva & Wood (2013; 2015) for a range of pressures (0.5 to 2 GPa) and temperatures (1300 to 1500^{o} C). Other than the experiments performed at 2 GPa, the rest were deemed unsatisfactory due to the loss of material, sometimes resulting in an empty capsule or a glass without sulfides. These issues should be relatively straightforward to fix by modifying the fitting of the pieces in the sample cell, and by increasing the sample pressure to the goal pressure before applying heat to the sample, when conducting <1 GPa experiments.

The samples performed at 2 GPa were successful and therefore, I calculated their sulfide-silicate partitioning coefficients for all the elements of interest. These partitioning coefficients showed trends that were mostly in agreement with the behaviour that Kiseeva & Wood (2015) predicted for an increase in temperature

(Figure 6 & 7). This suggests that the effect of pressure must be subordinate to that of temperature for most elements.

Nonetheless, Ni's partitioning coefficient did not change with the increasing temperature, as opposed to the pronounced decrease it had been described to experience in Kiseeva & Wood (2015). Since my experiments were performed at a higher pressure than those in Kiseeva & Wood (2015), the effect of temperature might have been counteracted by that of the pressure, as described in Kegler *et al.* (2008) and Fischer *et al.* (2015) for the Fe—Ni exchange reaction., albeit this occurred at higher pressures (>3 GPa). In addition to this, the $D_{Zn}^{sulf/sil}$ calculated from the measured concentrations in the sample SSP15-2 was ~350% higher (Figure 7) than the value obtained from the sulfide-silicate partitioning coefficient calculator developed by Kiseeva & Wood (2015). The reason for this might again be the difference in pressure between the two studies.

Thus, it is necessary to expand this pressure series to a larger range of pressures, both lower and higher than 2 GPa, to explore the potential deviations from the predictions, and successfully implement the pressure parameter into our partitioning models.

Chapter 5. Sulfide silicate partitioning of mercury.

As a chalcophile, mercury shows affinity for the sulfide phase, however, due to the experimental difficulties of working with mercury, there is no quantitative experimental data on its sulfide-silicate partition coefficients. While its occurrence in nature suggests that mercury should be strongly chalcophile, since it is mostly found in the form of HgS, this is yet to be properly supported by empirical data. In this section, we performed sulfide-silicate partitioning experiments between a HgO bearing Icelandic basalt rock powder mixed with FeS. We also observed the Hg exchange between two types of silicate mixtures when in contact with a thin layer of HgS. The goal of these experiments is to evaluate whether the runtime has any impact on the retention of mercury for the given experimental conditions and examine the potential outcome when the mercury source is HgS. The samples will be named after their starting silicate and sulfide composition with the prefixes and suffixes “IB”, “Hg", “FeS”, “HgS”, “TS”, and 2 digits for runtime in minutes.

5.1. Methods.

5.1.1. Single capsule method: Effect of run time in the distribution of Hg or “IBFeS” time series and success at mercury retention.

In the same manner as the SSP suite (chapter 4, section 4.2.1), we created a new mixture “IBC4” by adding 30 wt. % FeS powder to the existing composition “IBC3” (IB with 1000 ppm of both HgO and Tl_2O_3) to check the behaviour of Hg in the presence of sulfides. We produced two glasses (Table 1 & Table 2): IBFeS10 (10-minute run), and IBFeS40 (40-minute run). These experiments were run at 1425ºC

and 1.5 GPa, using the same sample cell as for A001, with a 6 mm O.D., 4 mm I.D. graphite capsule but a thin 12.5 mm O.D. and 10 mm I.D. NaCl outer sleeve and a Pyrex 8 mm I.D. tube as an inner sleeve (Figure 1. e). Afterwards, we recovered the glass from the capsule and manually separated the sulfide phases from the silicate glass.

We also ran two additional piston-cylinder experiments, containing 10% HgS at the bottom of the capsule, and the mixtures IBC4 and IBC5 (Icelandic basalt with 1000ppm Tl_2O_3, see Table 1), respectively (Figure 1. f, g). Once again, the sample assembly consisted of a thin NaCl sleeve, a pyrex tube, a MgO-packed graphite furnace, and a 6 mm O.D., 4 mm I.D. graphite capsule. These experiments were run at the same temperature and pressure conditions (1425º C, 1.5 GPa), for 20 minutes each. The glass produced from the IBC4 mixture —and therefore containing two types of sulfides— was named “IBFeSHgS20” and the one containing derived from the single-sulfide experiment was named “IBHgS20”.

For all the produced glasses, we mounted both sulfide and glass in epoxy, polished it with synthetic diamond particles, and carbon-coated it to be observed *via* the Electron Microprobe (EMP; CAMECA SX-5 FE) at the University of Oxford, Earth Sciences Department. The remaining glass was carefully cleaned from any potential sulfide inclusion, sonicated, and ground down to <354 µm to determine the Hg concentration remaining in the glass through direct analysis with Lumex.

5.2. Results and discussion.

5.2.1. Major element analysis: single capsule IBFeS time series and HgS-disc experiments.

We proceeded similarly as with the SSP-suite for the analysis of sulfide phases in single capsule IBFeS time series, as well as for those experiments that contained HgS discs. The sulfide phases of the IBFeS time series were characterised through WDS point analysis, at 15 kV and ~19 nA beam current. We used a 1-µm spot size due to the limited available surface. The standards used were andradite for Fe, pyrite for S, and cinnabar for Hg. Peak counting times were 30 s, 30 s, and 120 s, respectively.

The standard deviation for the IBFeS experiments was 1 for Fe, 0.45 for S, and 0.32 for Hg, and the average Hg measured was 622.34 ppm and 694.36 ppm for the 10 min and 40 min experiments respectively. These Hg concentrations are below detection limits (3700 ppm) for this analysis, so their comparison would be unreliable.

IBHgS20, which had a starting Hg concentration of 8.6 wt %, recorded a Hg concentration of 315.22 ppm, again, below detection limits. The experiment IBFeSHgS20 had no retrievable sulfide (microscopic inclusions in the silicate glass).

5.2.2. Total mercury content analysis: capsule IBFeS time series and HgS-disc experiments.

All the glasses were analysed with the Lumex Mercury analyzed as previously described in chapter 3 section 2 The single-time measurements were 74 ppb and 10 ppb for the 10 minutes long and the 40-minute-long experiments respectively. This, ignoring the unreliable amounts of the sulfide analysis, results in a percentage of >99.99 over the initial Hg input that is missing from the samples (Table 2). On top of that, due to the mentioned difficulties when separating the sulfide and silicate phases, the presence of Hg-enriched sulfide inclusions in the glass might be responsible for the higher concentration recorded for the 10-minute-long experiment.

The silicate glass of the experiment IBHgS had an initial Hg concentration of 8.6 wt %, which despite the great loss of mercury experienced during the experimental run and the smaller than usual mass input into the Lumex device (8.2 mg, instead of the usual ~16 mg), released too much mercury for the analyser to bear, and triggered a low radiation warning from the detector. In this case, the measurement is assumed to be invalid and should be repeated, however, for the sample IBHgS20, this was not possible since all the mass was used up at once. Given these circumstances, this sample was not included in the calculations or datasets.

The silicate glass of the IBFeSHgS (original input of ~8.6 wt %), was measured several times, using sample masses from 0.6 to 2.2 mg, and produced an average concentration of 91.55 ppm (Table 2), but a significant inconsistency in measurements (standard deviation of 37.65 ppm).

5.3. Double-capsule method, “NiC” experiments: Attempt at minimising Hg loss.

Due to the difficulties in separating the scattered microscopic inclusions of sulfide in the prior Hg—S glasses (chapter 5, section 5.2.1), we added an inner graphite capsule to act as a physical barrier that should gather all the sulfide phases in the same region of the assembly. For this, we loaded a graphite capsule with a mixture of HgS and FeS, and put it inside a larger Nickel capsule, of which the remaining spaces between the two capsules would be filled with silicate rock powder The porosity of the graphite capsule should allow the migration of Hg through the two regions, while keeping the sulfide within the restricted graphite area, therefore making it easier to separate and analyse. The outer nickel capsule should offer a stronger seal than that of the graphite capsule used in the former experiments. The products of these experiments are named after the composition of the capsules, NiC and followed by a digit indicating the run number.

5.3.1. Methods.

The starting materials for the silicate were Icelandic basalt and $CaCl_2$ at 3 wt. %. The addition of Cl to the initial composition will cause a depression in the liquidus (Filiberto & Treiman 2009a; Filiberto *et al.*, 2014) and therefore allow for lower experimental temperatures. The sulfide consisted of a mixture of FeS with HgS at 5 wt. %. ~43,000 ppm Hg (Table 3).

Amounts of 2-3 mg of silicate were loaded at the bottom of the Ni capsules 6 mm O.D. and 3 mm I.D., and the sulfide was packed in a graphite capsule of 3 mm O.D.

and 1 mm I.D. The lid of the Ni capsule was polished to ensure full contact between the pieces of the capsule. The Ni capsule should be pressure-welded during the experiment, sealing the capsule, providing a closed environment for the sample, while not forming an amalgam with Hg for the intended temperature range (Jangg & Lugscheider 1973).

The nickel capsule was supported by Al_2O_3 pieces, in the same way as the sulfide-silicate experiments, with an alumina ring surrounding it. The assembly was tightly packed inside a graphite furnace and protected by a CaF_2 sleeve (Figure 1. i). The sample cells were wrapped in Pb foil in the same way as in the former experiments.

The samples were melted at 1200 °C and 1 GPa for 1h and quenched by turning the power off at the run pressure in the same way as the SSP suite (cooling rates of 40-30 °C/s up to reaching 100 °C). The pressure was released slowly after a temperature below 40 °C was reached. The products were mounted in epoxy resin and hand-polished to show a cross-section of the inside of the capsules. The inner capsules were filled with a silvery sulfide phase, while the bottom of the nickel capsules contained black silicate glass. The silicate was physically separated by cutting the sample and carving it out of the capsule with a small chisel. The sample NiC1 contained graphite particles belonging to the bottom of the inner capsule and had a heterogeneous appearance in particle size, which was due to a first attempt to chisel out the material, while accidentally extracting some of the graphite capsule surrounding it, which mixed with the silicate particles extracted. No further grinding or separation of this sample was carried out due to the risk of losing the

small mass fraction that was recovered. NiC2 was released from the capsule by fracturing the silicate into big pieces, by using a manual die-press. The NiC2 glass was ground down to a very fine powder for analysis in the Lumex Direct Mercury analyser. The sulfide phases within the Ni capsule were further polished down to 1 micron, carbon-coated and analysed through EMP imaging.

5.3.2. Results and discussion.

A) Analysis of the major elements of the NiC sulfides.

The sulfides phases from the NiC1 and NiC2 experiments were first analysed at the same time as those of the SSP-suite, using the same settings and standards (including cinnabar).

Table 8. Major elements for the sulfide phase in the NiC experiments in wt. %

Run No.	NiC2*	σ	NiC2	σ	NiC1*	σ	NiC1	σ
n	3		13		7		30	
D.L.	0.6	n.a.	2.2	n.a.	0.6	n.a.	2.2	n.a.
O	n.m.	n.m.	1.76	1.17	n.m.	n.m.	1.58	2.25
Ni	2.15	0.27	n.m.	n.m.	33.65	21.56	n.m.	n.m.
S	33.13	1.79	35.64	1.38	18.87	9.28	27.46	6.54
Hg	0.14	0.06	0.27	0.55	0.55	0.30	0.79	0.68
Fe	59.60	0.51	61.79	0.41	42.11	12.99	46.33	6.36
Total	95.02	1.54	99.46	0.74	95.19	5.55	76.16	10.76

* Second measurement. – D.L. ~ Detection Limits.

The sulfide NiC1 presented a heterogenous texture consisting of a mesh of three types of differently coloured vermicular and rounded shapes which may represent the formation and intergrowth of phases during quench (Figure 8. a.). NiC2

presented a clean homogenous surface with a few lighter-coloured submicron-sized spots (Figure 8. b.).

The elemental concentrations for the major elements of the sulfide (Table 8) are coherent with those of the SSP suite (Table 6), but the mercury concentrations measured with the WDS analysis were much lower (<0.79 wt. %, table 8) than the detection limits for this element, 2.2 wt. %. Therefore, we carried out a second analysis of the NiC sulfides, optimizing the collection routine for Hg. We used a large area analysing crystal (LLIF), prolonged the dwell time to 90 seconds, and the electron beam current was increased from 40 nA to 120 nA, to improve the count rate and sensitivity of the analysis. These changes allowed us to reduce the detection limits to ~6000 ppm for mercury. We also included Ni in our analysis to detect any communication between the capsule and the sample. The results for the sulfides (Table 8) show totals around 95 %, which are likely to express the presence

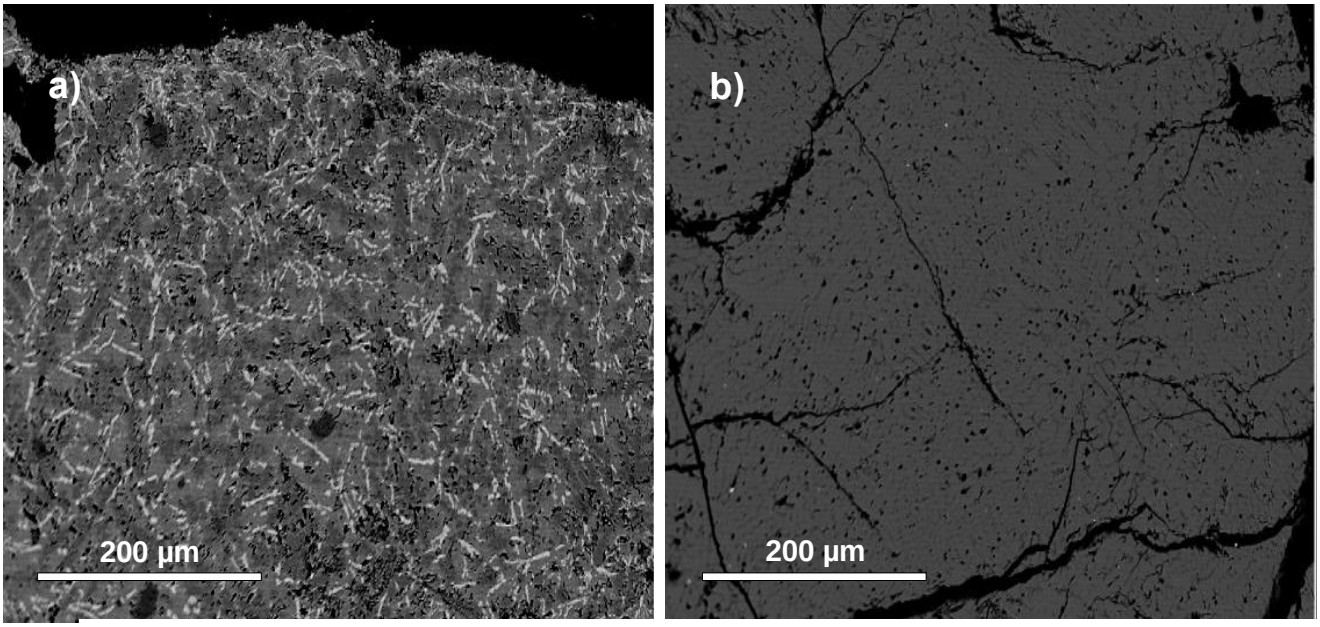

Figure 8. BSE images of the sulfide phases formed in both NiC1(a) and NiC2 (b).

of around <2-3 wt. % O (data obtained from the previous measurement that included O). The measured mercury concentrations were still below detection limits (5500 ppm for NiC1, and 1400 ppm for NiC2).

Regarding the composition of the different phases observed in NiC1. The sample consists of a medium grey surface with brighter metallic phases and big darker regions (Figure 8. a). The analytical results show that the medium grey background is a nickel-iron sulfide with variable amounts of Ni and Fe, in and minimal amounts of Hg (28.10 wt. % S, 28.94 wt.% Ni, 0.40 wt. % Hg, and 40.03 wt. % Fe). The lighter phase showed a high concentration of Fe and Ni, as well as low S (10.04 wt.% S, 49.04 wt.% Ni, 0.81 wt.% Hg, and 37.35 wt.% Fe). Uniquely, this metallic phase had Hg measurements above detection limits. The darkest phase was iron-rich and had a moderate amount of sulfur, which implies a combination of iron, sulfur, and oxygen (17.78 wt. % S, 1.61wt.% Ni, 0.25 wt.% Hg, and 62.64 wt.% Fe). This phase also produced low totals of 82 wt. %, which probably relates to the presence of a significant amount of oxygen.

Furthermore, we performed a transverse line across the lid of each one of the nickel capsules, to evaluate the degree of Hg migration into the nickel capsule. We set Ni as the matrix, which allowed us to increase the beam current to a ~500 nA beam current for Hg, thus lowering the detection limits to 2800 ppm.

The line analysis showed a small increase in mercury next to the inside of the capsule ~0.3 wt.% for both capsules, which is barely above detection limits, and there was no coherent diffusion gradient through the transverse. On the other hand,

Fe did show a concentration of almost 3 wt. % on the inner border of the lid, and a rapid decrease towards the outermost part of the capsule. The graphite capsule also presented visible fissures filled with nickel-iron sulfide that connect the nickel capsule with the core of the graphite capsule (Figure 9). The double-capsule samples failed to retain mercury, as the concentrations detected were all below, or barely above the detection limits, and inconsistent throughout the samples. However, given that the actual mercury mass input in the sample was originally 0.012 mg, Hg might have been dissolved into Ni through the entire capsule-system since a measurable, yet small amount of mercury was collected in the metallic capsule, together with the Ni bearing sulfide product, and in the metallic Ni-Fe alloys found in the experiment NiC1. Assuming that ideally, Hg had been distributed homogeneously through the capsule walls, sulfide, and silicate phases, the amount

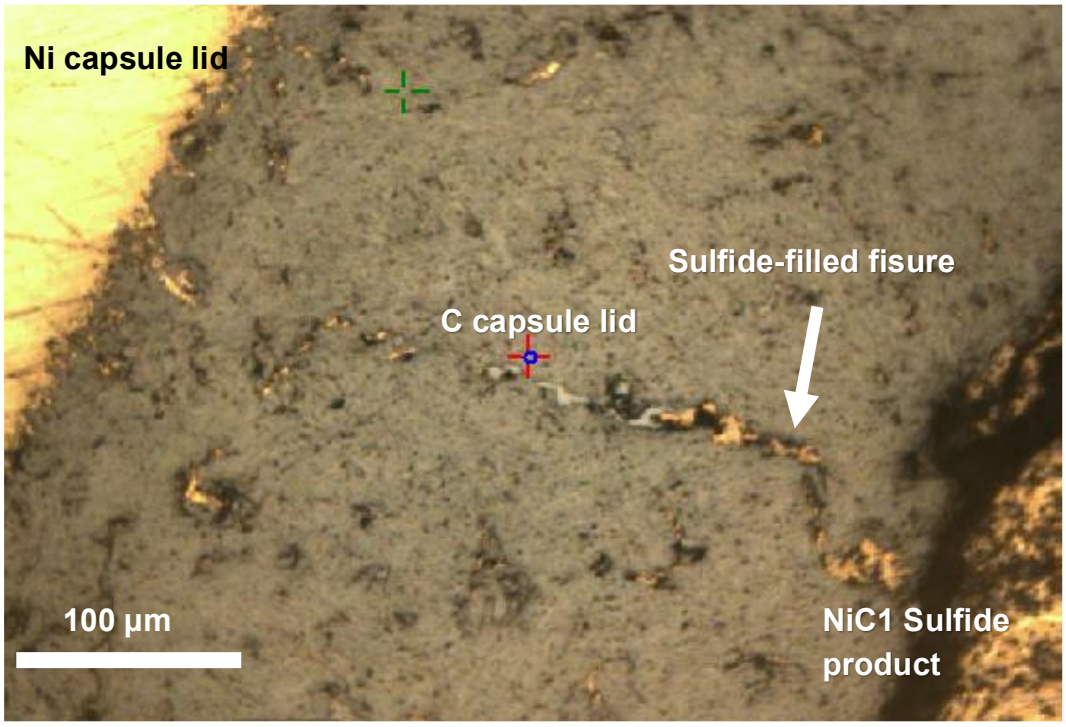

Figure 9. Reflected light photomicrograph of a fissure breaking through the lid of the graphite capsule in sample NiC1.

of Hg anywhere in the capsule could not have been higher than 412 ppm. This number is much smaller than any of the detection limits achieved in our past routines. To overcome these obstacles of detecting Hg through WDS analysis, we could increase the amount of mercury added to the sulfide mixture. Additionally, we could test the actual phenomena occurring within the nickel capsule, by loading a graphite capsule with HgS alone, to evaluate the degree of Hg migration into the nickel without the interference of other elements like Fe.

B) Total mercury content analysis: double-capsule experiments.

The silicate produced with the nickel-graphite capsule assembly also experienced a Hg loss of > 99.99 % from the original input of 4.3 wt. %. The silicate glass produced in the double capsule experiments, was clear of sulfide phases, due to the small mass recovered for the experiments, we could only collect one measurement. NiC1 produced two peaks followed by a long tail and recorded 41.2 ppm Hg (Table 2). The double peak graph could be related to the heterogeneity of the particles as speculated in Bin *et al.* (2001) or to be linked to the multi-stepped thermal decomposition of the mercurous compounds (Lopez-Anton *et al.,* 2010; Liu *et al.,* 2013), however, the reason behind this is still debated. NiC2 produced a small peak and recorded 1.2 ppm Hg.

The concentration of mercury for the double-capsule experiments was very low in both silicate and sulfide. Considering that mercury is expected to favour sulfide in these conditions, the lack of a significant amount of mercury in the sample must

mean that the mercury escaped the sample, either by degassing during the experimental run or by being dispersed through the Ni. While this capsule setup was promising in its potential to keep very volatile elements inside at high temperatures, Hg might have dissolved into the nickel capsule, reducing the concentration of this element within the silicate and the sulfide phases. A test with only HgS as starting material within the double capsule should be performed to observe the actual communication between Hg and Ni.

It is also important to consider that due to the capsule being pressure-welded during the experiment, instead of manually welded before the run, the sealing of this might not have been perfect, allowing the mercury to escape the assembly. If this were determined as the issue, the solution would be to ensure a perfectly clean and polished contact surface between the lid and the body of the capsule.

5.4. Summary and further thoughts.

I completed a number of partitioning experiments between silicate mixtures —with and without HgO— and a sulfide liquid. Two main sample cell types were used, one with a single capsule, and another with a double capsule.

The single capsule experiments were unsuccessful at segregating the sulfide phase and the silicate glass, with a high dispersion of sulfide inclusions of even microscopic size being present in all glasses. IBFeSHgS20 did not have any sulfide that could be large enough to be manually separated. Therefore, because of the

potential presence of sulfide inclusions in the silicate glasses, the total mercury analyses might have shown slightly Hg enriched concentrations. Nevertheless, the measured Hg concentrations for the silicate glasses were 74 ppb and 10 ppb for the 10 minutes long and the 40-minute-long IBFeSTS experiments, respectively (Table 2). The Hg concentrations measured in the sulfides was of ~622 ppm (IBFeSTS10) and 694 ppm (IBFeSTS40). Despite these being over 60% of the initial mercury input in the mixture —1000 ppm— they were still below detection limits (3700 ppm) and we cannot make use of these data for partitioning calculations. Achieving low enough Hg detection limits during a WDS analysis is an important obstacle to overcome since we should be looking at concentrations of mercury significantly below 3700 ppm. This could be pursued during future analyses by increasing the electron beam current, dwell time, and by using a large area analysing crystal.

The double-capsule experiments were designed to prevent the sulfide dispersion present in the single-capsule experiments and to add an external metallic seal that might be more successful at preventing mercury loss. While this assembly succeeded at keeping both phases separated, the silicate glass was difficult to extract from this double capsule set up, which increased the risk of losing material and contaminating the silicate. The obtained glass was scarce and hence the total mercury concentration measurements were limited. These concentrations were 41.2 ppm for NiC1 and 1.2 ppm for NiC2 over an initial input of 1000 ppm Hg (Table *2*). The causes for this disparity are discussed in section B. The sulfide

measurements were again below detection limits (6000 ppm), despite our efforts to decrease them by modifying our routine.

Ultimately, it is important to test the interaction between Hg and Ni at >1000^{o} C, since we cannot assume with confidence that mercury will not dissolve into the Ni capsule walls during the experiment — See section A.

Chapter 6. Conclusions and further work

6.1. Best analytical technique to perform total mercury content analysis

When analysing trace elements like mercury, LA-ICP-MS is one of the most popular techniques. While we obtained some promising correlation for the samples containing >100 ppm Hg, the ones with lower concentrations produced worse linear regressions (Figure 2).

Mercury is an element with higher ionisation energy (10.6 kJ mol^{-1}) than most other elements that are routinely analysed with LA-ICP-MS, meaning that the capacity of the argon plasma to ionise Hg is relatively low — the ionisation potential of argon is 15.76 kJ mol^{-1}. Furthermore, Hg has seven stable isotopes, which decreases the concentration available per single isotope in proportion to their abundances, posing a challenge to detect the signal with any degree of accuracy and reproducibility. Considering the low concentration of Hg in basaltic systems and the low Hg retention values from this study, the potential presence of interferences for the isotopes ^{198}Hg, ^{199}Hg and ^{204}Hg, and the economic cost of this technique, the use of LA-ICP-MS does not seem to be the most suitable for mercury analysis.

As described in chapter 2, section 2, we tested several basaltic standards of which Hg concentration had been previously determined with the direct mercury analyser Milestone DMA-80, which includes an amalgamation step (Marie *et al.,* 2015). We performed the measurements *via* thermal decomposition assisted atomic absorption spectrometry with the Lumex RA-915+ multifunctional mercury analyser with

pyrolysis unit, at the University of Oxford. These analyses replicated almost perfectly the concentrations measured in Marie *et al.* (2015), proving to be the better technique to analyse mercury in the silicate due to its accuracy and reproducibility.

Ultimately, we observed the effect of grain size in the release of Hg through thermal decomposition in the Lumex analyser. Our results show that when using powdered samples of less than 354 µm grain size, the measured Hg concentrations appear consistently higher, however, these calibrations need to be more properly adjusted, with a larger data sample and a consideration of all statistical errors.

6.2. Issues with mercury loss in silicate and sulfide products.

We have attempted a series of experimental assemblies to produce synthetic Hg at high temperature (Figure 1), however, we have been unable to keep a consistent amount of mercury for any of these experimental set-ups. So far, experiment A002, which was run at a lower temperature (1375º C) and using CaF_2 -sleeved sample cell, with Fe_2O_3 discs on top and bottom of the capsule had the smallest Hg loss overall (76.74 %, Hg concentrations over 80 ppm). Despite the big loss percentage in all the other samples (>99.9 % loss), we have still managed to retain several hundreds of ppb to tens of ppm for most samples (Table 2).

The results for Hg concentration in the time series, for both sulfide-bearing and silicate-only products, were not reliable due to bad linear correlation, large standard deviation of the measurements (Figure 3 & table 2), and/or extremely low concentrations obtained (Table 2).

The NiC method did not improve our Hg retention in any of the phases. This method might be problematic due to the Ni—Hg interaction, and therefore this should be studied separately, by reproducing the experiment with a HgS-only starting material. Additionally, we should carry out more experiments with this cell design, maybe at slightly higher pressures while improving the surface of contact between the Ni lid and the body of the capsule. Other metals like iron should also be considered as potential capsule materials.

If it were possible to satisfy the requirements of consistently preserving mercury for a number of sulfides and glasses so that the method used is reproducible, then it would be possible to undertake further experiments to assess the sulfide-silicate distribution of Hg, and attempt partition experiments under different compositions and sulfur- and oxygen-fugacities, but at this time, the main challenge is still the systematic retention of mercury in the samples. If successful, Hg-containing synthetic glasses will open a path to investigate mercury partitioning between silicate and sulfide melts.

Despite this handicap, any advancements on the high-temperature synthesis of mercury-bearing experimental glasses will contribute to establishing the basis for those experiments in the future, and therefore these attempts, failed or successful, are relevant to the study of mercury behaviour during volcanic degassing.

6.3. Effect of pressure and problems with successfully reproducing the Kiseeva and Wood (2013; 2015) methodology.

Regarding the sulfide-silicate partitioning experiments involving other chalcophile and lithophile elements, the 2GPa experiments of the SSP suite provided promising results that mostly agree with the Kiseeva & Wood (2015) model for the behaviour of the selected elements. Solving the contamination issues for the rest of the pressures should be quite straightforward, but in the case that the experimental runs at pressures <1 GPa continue to be unsatisfactory, we could aim to perform experiments at pressures >2 GPa; hence obtaining a valid range to estimate the effect of these over the distribution of trace-elements.

The results from these partitioning experiments will shed light on how pressure might be affecting the distribution of trace elements in sulfide-saturated igneous materials and thus improving the existing prediction models.

Ultimately, the analysis of multiple basaltic materials, with a focus on tholeiites (closest to LIP composition), by using the Lumex mercury analyser for Hg measurements, as well as the LA-ICP-MS for the rest of trace elements, and EMP for the major element composition will help to establish a catalogue of complete elemental data for Hg-bearing basalts. Databases including mercury measurements are very rare, and in most cases, when the mercury is included, trace-element analysis is lacking. These gaps prevent any possibility to compare other elements' behaviour to that of mercury during different magmatic/volcanic processes. By increasing this data, we would be able to apply statistical analysis to detect distribution patterns of different elements that might be behaving parallel to Hg. These patterns are necessary to find potential Hg proxy elements that might be

easier to measure but provide information regarding its behaviour. The existence of a proxy that has a greater presence in literature would facilitate the understanding of how Hg is affected by those processes and be used instead of mercury in high-temperature experiments when using mercury is not feasible.

References

Akella, J., Vaidya, S. N., & Kennedy, G. C. (1969). Melting of sodium chloride at pressures to 65 kbar. Physical Review, 185(3), 1135.

Algeo, T. J., & Liu, J. (2020). A re-assessment of elemental proxies for paleoredox analysis. Chemical Geology, 119549.

Allard, P., Aiuppa, A., Loyer, H., Carrot, F., Gaudry, A., Pinte, G., ... & Dongarrà, G. (2000). Acid gas and metal emission rates during long-lived basalt degassing at Stromboli volcano. Geophysical Research Letters, 27(8), 1207-1210.

ATSDR. Toxicological Profile for mercury. Atlanta, GA: Agency for Toxic Substances and Disease Registry, US Public Health Service, 1999.

ATSDR. Toxicological Profile for mercury. Atlanta, GA: Agency for Toxic Substances and Disease Registry, US Public Health Service, 1999.

Bagnato, E., Aiuppa, A., Parello, F., Allard, P., Shinohara, H., Liuzzo, M., & Giudice, G. (2011). New clues on the contribution of Earth's volcanism to the global mercury cycle. Bulletin of Volcanology, 73(5), 497-510.

Bagnato, E., Aiuppa, A., Parello, F., Calabrese, S., D'alessandro, W., Mather, T. A., ... & Wängberg, I. (2007). Degassing of gaseous (elemental and reactive) and particulate mercury from Mount Etna volcano (Southern Italy). Atmospheric Environment, 41(35), 7377-7388.

Bagnato, E., Barra, M., Cardellini, C., Chiodini, G., Parello, F., & Sprovieri, M. (2014). First combined flux chamber survey of mercury and CO2 emissions from

soil diffuse degassing at Solfatara of Pozzuoli crater, Campi Flegrei (Italy): Mapping and quantification of gas release. Journal of volcanology and geothermal research, 289, 26-40.

Bagnato, E., Tamburello, G., Avard, G., Martinez-Cruz, M., Enrico, M., Fu, X., ... & Sonke, J. E. (2015). Mercury fluxes from volcanic and geothermal sources: an update. Geological Society, London, Special Publications, 410(1), 263-285.

Banerjee, D., Joseph, A., Sudarsan, V. K., Wattal, P. K., & Das, D. (2012). Effect of composition and temperature on volatilization of Cs from borosilicate glasses. Journal of the American Ceramic Society, 95(4), 1284-1289.

Bargagli, E., Monaci, F., Bianchi, N., Bucci, C., & Rottoli, P. (2008). Analysis of trace elements in bronchoalveolar lavage of patients with diffuse lung diseases. Biological trace element research, 124(3), 225.

Bin, C., Xiaoru, W., & Lee, F. S. (2001). Pyrolysis coupled with atomic absorption spectrometry for the determination of mercury in Chinese medicinal materials. Analytica Chimica Acta, 447(1-2), 161-169.

Bond, D. P. G., & Grasby, S. E. (2017). On the causes of mass extinctions: Palaeogeography, Palaeoclimatology, Palaeoecology, v. 478.

Boyd, F. R., & England, J. L. (1960). Apparatus for phase-equilibrium measurements at pressures up to 50 kilobars and temperatures up to 1750° C. Journal of Geophysical Research, 65(2), 741-748.

Brooker, R., Holloway, J. R., & Hervig, R. (1998). Reduction in piston-cylinder experiments: The detection of carbon infiltration into platinum capsules. American Mineralogist, 83(9-10), 985-994.

Canil, D., Crockford, P. W., Rossin, R., & Telmer, K. (2015). Mercury in some arc crustal rocks and mantle peridotites and relevance to the moderately volatile element budget of the Earth. Chemical Geology, 396, 134-142.

Chan, T. Y., Chan, A. P., & Tang, H. L. (2020). Nephrotic syndrome caused by exposures to skin-lightening cosmetic products containing inorganic mercury. Clinical Toxicology, 58(1), 9-15.

Clapham, M. E., & Renne, P. R. (2019). Flood basalts and mass extinctions. Annual Review of Earth and Planetary Sciences, 47, 275-303.

Coufalík, P., Krmíček, L., Zvěřina, O., Meszarosová, N., Hladil, J., & Komárek, J. (2018). Model of mercury flux associated with volcanic activity. Bulletin of environmental contamination and toxicology, 101(5), 549-553.

Crump, K.S., Kjellstrom, T., Shipp, A.M., Silvers, A. and Stewart, A. 1998. Influence of prenatal mercury exposure upon scholastic and psychological test performance: benchmark analysis of a New Zealand cohort. Risk Anal. 18, 701–713.

Edwards, B. A., Kushner, D. S., Outridge, P. M., & Wang, F. (2020). Fifty years of volcanic mercury emission research: knowledge gaps and future directions. Science of The Total Environment, 143800.

F.L Fertonani, A.V Benedetti, J Servat, J Portillo, F Sanz, Electrodeposited thin mercury films on Pt–Ir alloy electrodes, Thin Solid Films, Volume 349, Issues 1–2, 1999, 147-154, ISSN 0040-609

Fabio Barbone, F., Valent, F., Pisa1, F., Daris, F., Fajon, V., Gibicar, D., Logar, M. and Horvat, M. 2004. Prenatal low-level methyl mercury exposure and child development in an Italian coastal area. Seychelles Medical and Dental Journal. 7, 149–154.

Ferrara, R., Mazzolai, B., Lanzillotta, E., Nucaro, E., & Pirrone, N. (2000). Volcanoes as emission sources of atmospheric mercury in the Mediterranean basin. Science of the Total Environment, 259(1-3), 115-121.

Fertonani, F. L., Benedetti, A. V., Servat, J., Portillo, J., & Sanz, F. (1999). Electrodeposited thin mercury films on Pt–Ir alloy electrodes. Thin Solid Films, 349(1-2), 147-154.

Filiberto, J., & Treiman, A. H. (2009). The effect of chlorine on the liquidus of basalt: First results and implications for basalt genesis on Mars and Earth. Chemical Geology, 263(1-4), 60-68.

Filiberto, J., Dasgupta, R., Gross, J., & Treiman, A. H. (2014). Effect of chlorine on near-liquidus phase equilibria of an Fe–Mg-rich tholeiitic basalt. Contributions to Mineralogy and Petrology, 168(1), 1-13.

Fischer, R. A., Nakajima, Y., Campbell, A. J., Frost, D. J., Harries, D., Langenhorst, F., ... & Rubie, D. C. (2015). High pressure metal–silicate partitioning of Ni, Co, V, Cr, Si, and O. Geochimica et Cosmochimica Acta, 167, 177-194.

Fostier, Anne & Melendez-Perez, Jose. (2013). Assessment of Direct Mercury Analyzer (R) to Quantify Mercury in Soils and Leaf Samples. Journal of the Brazilian Chemical Society. 24. 1880. 10.5935/0103-5053.20130235.

Granite, E. J., & Pennline, H. W. (2006). U.S. Patent No. 7,033,419. Washington, DC: U.S. Patent and Trademark Office.

Grasby, S. E., Beauchamp, B., Bond, D. P., Wignall, P. B., & Sanei, H. (2016). Mercury anomalies associated with three extinction events (Capitanian crisis, latest Permian extinction and the Smithian/Spathian extinction) in NW Pangea. Geological magazine, 153(2), 285-297.

Harada, M. 1978. Congenital Minamata disease: intrauterine methylmercury poisoning. Teratology 18, 285–288.

Heikens, A., Peijnenburg, W. J. G. M., & Hendriks, A. J. (2001). Bioaccumulation of heavy metals in terrestrial invertebrates. Environmental Pollution, 113(3), 385-393.

Higueras, P., Oyarzun, R., Lillo, J., & Morata, D. (2013). Intraplate mafic magmatism, degasification, and deposition of mercury: The giant Almadén mercury deposit (Spain) revisited. Ore Geology Reviews, 51, 93-102.

Hinkley, T. K., Lamothe, P. J., Wilson, S. A., Finnegan, D. L., & Gerlach, T. M. (1999). Metal emissions from Kilauea, and a suggested revision of the estimated worldwide metal output by quiescent degassing of volcanoes. Earth and Planetary Science Letters, 170(3), 315-325.

Holloway, J. R., & Wood, B. J. (2012). Simulating the Earth: experimental geochemistry. Springer Science & Business Media.

Jackson, A. C. (2018). Chronic neurological disease due to methylmercury poisoning. Canadian Journal of Neurological Sciences, 45(6), 620-623.

Jangg, G., & Lugscheider, E. (1973). Die Löslichkeit von Quecksilber in verschiedenen Metallen. Monatshefte für Chemie/Chemical Monthly, 104(5), 1269-1275.

Jones, M. T., Percival, L. M., Stokke, E. W., Frieling, J., Mather, T. A., Riber, L., ... & Svensen, H. H. (2019). Mercury anomalies across the Palaeocene–Eocene thermal maximum. Climate of the Past, 15(1).

Kegler, P., Holzheid, A., Frost, D. J., Rubie, D. C., Dohmen, R., & Palme, H. (2008). New Ni and Co metal-silicate partitioning data and their relevance for an early terrestrial magma ocean. Earth and Planetary Science Letters, 268(1-2), 28-40.

Kim, K. H., Mishra, V. K., & Hong, S. (2006). The rapid and continuous monitoring of gaseous elemental mercury (GEM) behavior in ambient air. Atmospheric Environment, 40(18), 3281-3293.

Kiseeva, E. S., & Wood, B. J. (2013). A simple model for chalcophile element partitioning between sulphide and silicate liquids with geochemical applications. Earth and Planetary Science Letters, 383, 68-81.

Kiseeva, E. S., & Wood, B. J. (2015). The effects of composition and temperature on chalcophile and lithophile element partitioning into magmatic sulphides. Earth and Planetary Science Letters, 424, 280-294.

Koizumi, S., Hiraga, T., Tachibana, C., Tasaka, M., Miyazaki, T., Kobayashi, T., ... & Sano, S. (2010). Synthesis of highly dense and fine-grained aggregates of mantle composites by vacuum sintering of nano-sized mineral powders. Physics and Chemistry of Minerals, 37(8), 505-518.

Landis, M. S., Keeler, G. J., Al-Wali, K. I., & Stevens, R. K. (2004). Divalent inorganic reactive gaseous mercury emissions from a mercury cell chlor-alkali plant and its impact on near-field atmospheric dry deposition. Atmospheric Environment, 38(4), 613-622.

Li, J., & Agee, C. B. (1996). Geochemistry of mantle–core differentiation at high pressure. Nature, 381(6584), 686-689.

Liu, X., Wang, S., Zhang, L., Wu, Y., Duan, L., & Hao, J. (2013). Speciation of mercury in FGD gypsum and mercury emission during the wallboard production in China. Fuel, 111, 621-627.

Liu, YongSheng, et al. "Applications of LA-ICP-MS in the elemental analyses of geological samples." Chinese Science Bulletin 58.32 (2013): 3863-3878.

Lopez-Anton, M. A., Yuan, Y., Perry, R., & Maroto-Valer, M. M. (2010). Analysis of mercury species present during coal combustion by thermal desorption. Fuel, 89(3), 629-634.

Ma, Z., Wood, C. W., & Bransby, D. I. (2001). Impact of row spacing, nitrogen rate, and time on carbon partitioning of switchgrass. Biomass and Bioenergy, 20(6), 413-419.

Marie, B., Marin, L., Martin, P. Y., Gulon, T., Carignan, J., & Cloquet, C. (2015). Determination of mercury in one hundred and sixteen geological and environmental reference materials using a direct mercury analyser. Geostandards and Geoanalytical Research, 39(1), 71-86.

Mason, R. P., Fitzgerald, W. F., & Morel, F. M. (1994). The biogeochemical cycling of elemental mercury: anthropogenic influences. Geochimica et Cosmochimica Acta, 58(15), 3191-3198

Mather, T. A. (2015). Volcanoes and the environment: Lessons for understanding Earth's past and future from studies of present-day volcanic emissions. Journal of Volcanology and Geothermal Research, 304, 160-179.

Mather, T. A., Witt, M. L. I., Pyle, D. M., Quayle, B. M., Aiuppa, A., Bagnato, E., ... & Ilyinskaya, E. (2012). Halogens and trace metal emissions from the ongoing 2008 summit eruption of Kīlauea volcano, Hawaii. Geochimica et Cosmochimica Acta, 83, 292-323.

McDade, P., Wood, B. J., Van Westrenen, W., Brooker, R., Gudmundsson, G., Soulard, H., ... & Blundy, J. (2002). Pressure corrections for a selection of piston-cylinder cell assemblies. Mineralogical Magazine, 66(6), 1021-1028.

Moore, G., Roggensack, K., & Klonowski, S. (2008). A low-pressure–high-temperature technique for the piston-cylinder. American Mineralogist, 93(1), 48-52.

Norris, C. A. (2016). Volatilities of trace elements in silicate melts (Doctoral dissertation, University of Oxford).

Norris, C. A., & Wood, B. J. (2017). Earth's volatile contents established by melting and vaporization. Nature, 549(7673), 507-510.

Olgun, N., Duggen, S., Andronico, D., Kutterolf, S., Croot, P. L., Giammanco, S., ... & Randazzo, L. (2013). Possible impacts of volcanic ash emissions of Mount Etna on the primary productivity in the oligotrophic Mediterranean Sea: Results from nutrient-release experiments in seawater. Marine chemistry, 152, 32-42.

Olumide YM, Akinkugbe AO, Altraide D, Mohammed T, Ahamefule N, Ayanlowo S, et al. Complications of chronic use of skin lightening cosmetics. Int J Dermatol 2008;47:344 – 353.

Outridge, P. M., Mason, R. P., Wang, F., Guerrero, S., & Heimburger-Boavida, L. E. (2018). Updated global and oceanic mercury budgets for the United Nations Global Mercury Assessment 2018. Environmental Science & Technology, 52(20), 11466-11477.

Percival, L. M. E., Witt, M. L. I., Mather, T. A., Hermoso, M., Jenkyns, H. C., Hesselbo, S. P., ... & Ruhl, M. (2015). Globally enhanced mercury deposition during the end-Pliensbachian extinction and Toarcian OAE: A link to the Karoo–Ferrar Large Igneous Province. Earth and Planetary Science Letters, 428, 267-280.

Percival, L. M., Jenkyns, H. C., Mather, T. A., Dickson, A. J., Batenburg, S. J., Ruhl, M., ... & Woelders, L. (2018). Does large igneous province volcanism always

perturb the mercury cycle? Comparing the records of Oceanic Anoxic Event 2 and the end-Cretaceous to other Mesozoic events. American Journal of Science, 318(8), 799-860.

Perrault, J. R. (2014). Mercury and selenium ingestion rates of Atlantic leatherback sea turtles (Dermochelys coriacea): A cause for concern in this species?. Marine environmental research, 99, 160-169.

Pirrone, N., Cinnirella, S., Feng, X., Finkelman, R. B., Friedli, H. R., Leaner, J., ... & Telmer, K. (2010). Global mercury emissions to the atmosphere from anthropogenic and natural sources. Atmospheric Chemistry & Physics, 10(13).

Pyle, D. M., & Mather, T. A. (2003). The importance of volcanic emissions for the global atmospheric mercury cycle. Atmospheric Environment, 37(36), 5115-5124.

Racki, G. (2020). A volcanic scenario for the Frasnian–Famennian major biotic crisis and other Late Devonian global changes: More answers than questions?. Global and Planetary Change, 103174.

Rudnick, R. L., and S. Gao. "Composition of the continental crust." The crust 3 (2003): 1-64.

Sanei, H., Grasby, S. E., & Beauchamp, B. (2012). Latest Permian mercury anomalies. Geology, 40(1), 63-66.

Schlüter, K. (2000). evaporation of mercury from soils. An integration and synthesis of current knowledge. Environmental Geology, 39(3-4), 249-271.

Smythe, D., Wood, B. & Kiseeva, E. (2017). The S content of silicate melts at sulfide saturation: New experiments and a model incorporating the effects of sulfide composition. American Mineralogist, 102(4), 795-803. https://doi.org/10.2138/am-2017-5800CCBY

Steenstra, E. S., Seegers, A. X., Eising, J., Tomassen, B. G. J., Webers, F. P. F., Berndt, J., ... & van Westrenen, W. (2018). Evidence for a sulfur-undersaturated lunar interior from the solubility of sulfur in lunar melts and sulfide-silicate partitioning of siderophile elements. Geochimica et Cosmochimica Acta, 231, 130-156.

Steenstra, E. S., Seegers, A. X., Putter, R., Berndt, J., Klemme, S., Matveev, S., ... & van Westrenen, W. (2020). Metal-silicate partitioning systematics of siderophile elements at reducing conditions: A new experimental database. Icarus, 335, 113391.

Takahata, N., HAYASHI, H., WATANABE, S., & ANSO, T. (1970). Accumulation of mercury in the brains of two autopsy cases with chronic inorganic mercury poisoning. Psychiatry and Clinical Neurosciences, 24(1), 59-69.

UNEP (United Nations Environment Programme). Global Mercury Assessment 2013: Sources, Emissions, Releases and Environmental Transport; UNEP Chemicals Branch: Geneva, Switzerland, 2013.

Vinodhini, R., & Narayanan, M. (2008). Bioaccumulation of heavy metals in organs of fresh water fish Cyprinus carpio (Common carp). International Journal of Environmental Science & Technology, 5(2), 179-182.

Vlach, S. R. F., Salazar-Naranjo, A. F., Torres-Corredor, J. S., Carvalho, P. R. D., & Mallmann, G. (2019). Calibration of high-temperature furnace assemblies for experiments between 200 and 600 MPa with end-loaded piston-cylinder apparatuses. Brazilian Journal of Geology, 49(1).

Wells, E. M., Herbstman, J. B., Lin, Y. H., Hibbeln, J. R., Halden, R. U., Witter, F. R., & Goldman, L. R. (2017). Methyl mercury, but not inorganic mercury, associated with higher blood pressure during pregnancy. Environmental research, 154, 247-252.

WHO. Elemental mercury and inorganic mercury compounds: human health aspects. Geneva, Switzerland, 2003, http://www.who.int/ipcs/ publications/cicad/en/cicad50.pd

Witt, M. L. I., Mather, T. A., Pyle, D. M., Aiuppa, A., Bagnato, E., & Tsanev, V. I. (2008). Mercury and halogen emissions from Masaya and Telica volcanoes, Nicaragua. Journal of Geophysical Research: Solid Earth, 113(B6).

Wojciechowski, M., Krata, A., & Bulska, E. (2008). Determination of mercury isotopic profile by inductively coupled plasma mass spectrometry: possibilities and limitations. Chem. Anal.(Warsaw), 53, 797-808.

Zhongting, M. A. (2001). Thermodynamic description for concentrated metallic solutions using interaction parameters. Metallurgical and Materials Transactions B, 32(1), 87-103.